Shaken and stirred: the Milky Way's dark substructures

Till Sawala,[1][*] Pauli Pihajoki,[1] Peter H. Johansson,[1] Carlos S. Frenk,[2]
Julio F. Navarro,[3][†] Kyle A. Oman[3] and Simon D. M. White[4]

[1]*Department of Physics, University of Helsinki, Gustaf Hällströmin katu 2a, FI-00014 Helsinki, Finland*
[2]*Institute for Computational Cosmology, Department of Physics, University of Durham, South Road, Durham DH1 3LE, UK*
[3]*Department of Physics and Astronomy, University of Victoria, 3800 Finnerty Road, Victoria, BC V8P 5C2, Canada*
[4]*Max-Planck Institute for Astrophysics, Karl-Schwarzschild-Straße 1, D-85741 Garching, Germany*

ABSTRACT

The predicted abundance and properties of the low-mass substructures embedded inside larger dark matter haloes differ sharply among alternative dark matter models. Too small to host galaxies themselves, these subhaloes may still be detected via gravitational lensing or via perturbations of the Milky Way's globular cluster streams and its stellar disc. Here, we use the APOSTLE cosmological simulations to predict the abundance and the spatial and velocity distributions of subhaloes in the range $10^{6.5}$–$10^{8.5}$ M$_\odot$ inside haloes of mass $\sim 10^{12}$ M$_\odot$ in Λ cold dark matter. Although these subhaloes are themselves devoid of baryons, we find that baryonic effects are important. Compared to corresponding dark matter only simulations, the loss of baryons from subhaloes and stronger tidal disruption due to the presence of baryons near the centre of the main halo reduce the number of subhaloes by $\sim 1/4$ to $1/2$, independently of subhalo mass, but increasingly towards the host halo centre. We also find that subhaloes have non-Maxwellian orbital velocity distributions, with centrally rising velocity anisotropy and positive velocity bias that reduces the number of low-velocity subhaloes, particularly near the halo centre. We parametrize the predicted population of subhaloes in terms of mass, galactocentric distance and velocities. We discuss implications of our results for the prospects of detecting dark matter substructures and for possible inferences about the nature of dark matter.

Key words: Local Group – cosmology: theory – dark matter.

1 INTRODUCTION

The Λ cold dark matter (hereafter ΛCDM) model explains many large-scale observations, from the anisotropy of the microwave background radiation (e.g. Wright et al. 1992) to the distribution of galaxies in the cosmic web (Davis et al. 1985), but inferences about the particle nature of dark matter or its possible (self-)interactions require observations on far smaller scales. Warm dark matter (WDM) particles, such as sterile neutrinos with masses of a few keV, have free-streaming scales of less than 100 kpc, and differ from CDM in terms of the halo mass functions at mass scales on the order of 10^9 M$_\odot$ and below (e.g. Avila-Reese et al. 2001; Bose et al. 2016), while weak self-interactions would produce shallow cores of the order of several kpc in the centre of dark matter haloes (e.g. Spergel & Steinhardt 2000). In principle, there is no shortage of observations that probe these small scales. They include the structures seen in the Lyman α forest (e.g. Croft et al. 2002; Viel et al. 2013), the abundance of dwarf galaxies in deep H I surveys (Tikhonov & Klypin 2009; Papastergis et al. 2011) and the abundance (e.g. Klypin et al. 1999; Boylan-Kolchin, Bullock & Kaplinghat 2011; Lovell et al. 2012; Kennedy et al. 2014) as well as internal kinematics that probe the density profiles (e.g. Walker & Peñarrubia 2011; Strigari, Frenk & White 2014) of Local Group dwarf galaxies.

While these studies have progressively narrowed the parameter space of viable dark matter candidates, inferences about the non-baryonic nature of dark matter from observations of the Universe's baryonic components are inherently limited by uncertainties in our understanding of complex astrophysical processes, such as radiative hydrodynamics, gas cooling, star formation, metal-enrichment, stellar winds, supernova and AGN feedback and cosmic reionization. For simple number counts, the effects of baryons in suppressing the formation of dwarf galaxies in CDM can be degenerate with the effects of WDM (e.g. Sawala et al. 2013). As of 2016, a plethora of studies have also offered baryonic solutions to the various problems for ΛCDM that had previously been identified in dark matter only (hereafter DMO) simulations (e.g. Okamoto, Gao & Theuns 2008;

[*] E-mail: till.sawala@helsinki.fi
[†] Senior CIfAR Fellow

Governato et al. 2010; Zolotov et al. 2012; Brooks et al. 2013; Arraki et al. 2014; Chan et al. 2015; Sawala et al. 2015; Dutton et al. 2016).

In addition, in the ΛCDM cosmological model, the majority of low-mass substructures that would most easily discriminate between different dark matter models are predicted to be completely dark (Bullock, Kravtsov & Weinberg 2000; Benson et al. 2002; Okamoto et al. 2008; Ocvirk et al. 2016; Sawala et al. 2016a), and hence unobservable through starlight. Fortunately, alternative methods exist that can reveal small structures and substructures purely through their gravitational effect and detect even pure dark matter haloes, thereby potentially breaking the degeneracy with baryonic physics.

(i) Gravitational lensing directly probes the projected mass distribution in and around galaxies and can reveal their luminous and non-luminous components. Weak gravitational lensing has confirmed the existence of massive dark haloes surrounding galaxies down to the Milky Way scales, or masses of $\sim 10^{12}\,\mathrm{M_\odot}$ (e.g. Mandelbaum et al. 2006). While these provide strong evidence for the existence of non-baryonic dark matter, they cannot distinguish between different currently viable models of cold, warm or self-interacting dark matter that deviate on mass scales below $\sim 10^9\,\mathrm{M_\odot}$. However, much lower masses, down to $\sim 10^6\,\mathrm{M_\odot}$, may be probed through strong gravitational lensing, either via flux-ratio anomalies (e.g. Mao & Schneider 1998; Xu et al. 2009, 2015), or detectable perturbations of observed Einstein rings by substructures in the lens itself or along the line of sight (Mao & Schneider 1998; Metcalf & Madau 2001; Dalal & Kochanek 2002; Vegetti et al. 2012, 2014). On these scales, different dark matter models may be clearly distinguished, provided that the expected abundances and distributions of substructures for different models can be reliably predicted.

(ii) Gaps in stellar streams originating from the tidal disruption of either globular clusters or dwarf galaxies can also provide evidence for substructures. In particular, globular cluster streams in the Milky Way, such as Palomar-5 (hereafter Pal-5, discovered by Odenkirchen et al. 2001) and GD-1 (discovered by Grillmair & Dionatos 2006), can be stretched out over many kpc along their orbit while conserving their phase-space volume. Compared to dwarf galaxies, globular clusters have much lower internal velocity dispersions resulting in much narrower streams, making them very sensitive tracers of both Galactic potential and perturbations by low-mass substructures (e.g. Ibata et al. 2002; Carlberg & Grillmair 2013). Based on the Vɪᴀ Lᴀᴄᴛᴇᴀ II DMO simulations, Yoon, Johnston & Hogg (2011) have calculated the interaction frequency of the Pal-5 stream with dark substructures during its assumed lifetime of 550 Myr; they predicted ~ 20 direct encounters with subhaloes of 10^6–$10^7\,\mathrm{M_\odot}$ and ~ 5 with subhaloes above $10^7\,\mathrm{M_\odot}$. Erkal & Belokurov (2015a,b) have computed the properties of predicted gaps in streams such as Pal-5 and GD-1 in ΛCDM. They show that the improved photometry, greater depth and more precise radial velocity and proper motion measurements of upcoming surveys such as *Gaia* (Perryman et al. 2001; Gilmore et al. 2012), DES (The Dark Energy Survey Collaboration 2005) and LSST (LSST Science Collaboration et al. 2009) should allow a characterization of perturbers in terms of mass, concentration, impact time and 3D velocity, for subhaloes above $10^7\,\mathrm{M_\odot}$, albeit with an irreducible degeneracy between mass and velocity. Recently, Bovy, Erkal & Sanders (2017) have used the density data of Pal-5 to infer the number of subhaloes in the mass range $M = 10^{6.5}$–$10^9\,\mathrm{M_\odot}$ inside the central 20 kpc of the Milky Way to be 10^{+11}_{-6}. However, they also noted the uncertainty

due to unaccounted baryonic effects and required assumptions in the subhalo velocity distribution.

(iii) The cold thin stellar disc of the Milky Way is another sensitive probe of the interactions with orbiting low-mass substructures. Satellite substructures passing through the Milky Way disc are expected to cause small but detectable changes in both radial and vertical velocity distribution of stars in the disc, resulting in a thickening of the thin disc (e.g. Toth & Ostriker 1992; Quinn, Hernquist & Fullagar 1993; Navarro & White 1994; Walker, Mihos & Hernquist 1996; Sellwood, Nelson & Tremaine 1998; Benson et al. 2004; Kazantzidis et al. 2008). The thinness and long-term stability of the Milky Way stellar disc could thus potentially put strong limits on the number of allowed massive dark substructures in the vicinity of the disc, and recent work by Feldmann & Spolyar (2015) suggests that the expected increase in the vertical velocity dispersion of disc stars due to the impact of dark substructures should be detectable with *Gaia*. However, it has been pointed out that internal processes such as turbulence and gravitational instabilities (e.g. Bournaud, Elmegreen & Martig 2009) and secular evolution (e.g. Schönrich & Binney 2009) can also lead to a thickening of the disc, while the vertical heating and thickening of the disc by dark substructures are severely reduced in simulations that include dissipational gas physics. The inclusion of gas reduces disc heating mainly through two mechanisms: the absorption of kinetic impact energy by the gas and/or the formation of a new thin stellar disc that can recontract heated stars towards the disc plane (e.g. Hopkins et al. 2009; Stewart et al. 2009; Moster et al. 2010).

While the above phenomena have a gravitational origin, they still fall short of providing a complete census of dark matter substructures. Instead, inferences about dark matter models based on the number of detected perturbations must be made statistically and, in each case, require an accurate prediction of the abundance, properties and distribution of dark matter substructures inside the central ~ 10–20 kpc of galaxy or group-sized dark matter haloes.

Previous work has relied on very high-resolution DMO simulations such as Vɪᴀ Lᴀᴄᴛᴇᴀ II (Diemand, Kuhlen & Madau 2007) and AQuᴀʀɪᴜs (Springel et al. 2008). These have shown that tidal stripping reduces the mass fraction of dark matter contained in self-bound substructures towards the halo centre (e.g. Springel et al. 2008). It has also been argued that the presence of a stellar disc and adiabatic contraction of the halo can lead to enhanced tidal disruption of substructures. Based on DMO simulations with an additional massive disc-like potential, D'Onghia et al. (2010) quantified the disruption of substructures through tidal stripping due to the smooth halo, tidal stirring near pericentre and 'disc shocking' by the passage of a substructure through the dense stellar disc. For their parameters, this led to a depletion of substructures by up to a factor of 3 for a subhaloes of mass $10^7\,\mathrm{M_\odot}$. Similarly, Yurin & Springel (2015) imposed a less massive disc inside a DMO simulation, and found a reduction in subhalo abundance by a factor of 2 in the centre, while Zhu et al. (2016) attributed some of the depletion of both dark and luminous subhaloes to similar effects.

In addition to the enhanced tidal disruption, the loss of baryons reduces the masses and abundances of low-mass subhaloes relative to DMO simulations (Libeskind et al. 2010; Romano-Díaz et al. 2010; Geen, Slyz & Devriendt 2013; Sawala et al. 2013, 2015; Schaller et al. 2015a). These earlier works have largely focused on the haloes of star-forming dwarf galaxies and include the effects of baryons inside them. Here, we focus on even lower mass subhaloes, and use high-resolution simulations that capture the full baryonic effects to explore the extent to which baryonic physics can change the

abundance of even completely dark substructures deeply inside the Milky Way (MW) halo, and discuss possible implications for the detection of substructures through lensing, stream gaps and disc heating.

This paper is organized as follows. In Section 2, we briefly describe the simulations used in this work, the selection of haloes and substructures and the reconstruction of orbits. In Section 3, we discuss how baryons affect the abundance and distribution of substructures inside dark matter haloes, as a function of satellite mass, galactocentric radius and time. In Section 4, we examine the subhalo energy, angular momenta, orbital velocity profiles and orbital anisotropy, and, in Section 5 we describe the non-Maxwellian subhalo velocity distributions. We discuss the implications of our results for different observables in Section 6, and conclude with a summary in Section 7. Additional details about the orbital interpolation and a comparison of the measured velocity distributions to standard Maxwellian fits are given in the appendix.

2 METHODS

We test the impact of baryons on substructures in Milky Way sized ΛCDM haloes by comparing cosmological simulations of Local Group analogues with and without baryons but otherwise identical initial conditions. In this section, we describe our simulations (Section 2.1), the identification of substructures (Section 2.2) and the reconstruction of their orbits (Section 2.3).

2.1 The APOSTLE simulations

Our results are based on *A Project Of Simulating The Local Environment* (APOSTLE; Sawala et al. 2016b), a suite of cosmological hydrodynamic zoom-in simulations of Local Group regions using the code developed for the *Evolution and Assembly of GaLaxies and their Environments* (EAGLE; Crain et al. 2015; Schaye et al. 2015) project. The simulations are performed in a *WMAP*-7 cosmology (Komatsu 2011), with density parameters at $z = 0$ for matter, baryons and dark energy of $\Omega_M = 0.272$, $\Omega_b = 0.0455$ and $\Omega_\lambda = 0.728$, respectively, a Hubble parameter of $H_0 = 70.4 \, \mathrm{km \, s^{-1} \, Mpc^{-1}}$, a power spectrum of (linear) amplitude on the scale of $8 \, h^{-1} \mathrm{Mpc}$ of $\sigma_8 = 0.81$ and a power-law spectral index $n_s = 0.967$. Regions were selected from a $100^3 \, \mathrm{Mpc^3}$ simulation (identified as DOVE in Jenkins 2013) to resemble the observed dynamical constraints in terms of distance and relative velocity between the MW and M31, and the isolation of the Local Group (Fattahi et al. 2016). Zoom initial conditions were constructed using the second-order Lagrangian perturbation theory (Jenkins 2010), at three different resolution levels, with gas (dark matter) particle masses of $\sim 1.0(5.0) \times 10^4 \, \mathrm{M_\odot}$ (labelled L1), $\sim 1.2(5.9) \times 10^5 \, \mathrm{M_\odot}$ (labelled L2) and $\sim 1.5(7.5) \times 10^6 \, \mathrm{M_\odot}$ (labelled L3), respectively. The gravitational softening lengths are initially fixed in comoving coordinates, and limited in physical coordinates to 134 pc, 307 pc and 711 pc. Except to check for convergence in Fig. 2, we only use the L1 simulations in this work. Each volume has also been resimulated as a DMO simulation, with identical initial conditions, and dark matter particle masses larger by a factor of $(\Omega_b + \Omega_{DM})/\Omega_{DM}$.

The EAGLE code is based on P-GADGET-3, an improved version of the publicly available GADGET-2 code (Springel 2005). Gravitational accelerations are computed using the Tree-PM scheme of P-GADGET-3, while hydrodynamic forces are computed with the smoothed particle hydrodynamics (SPH) scheme ANARCHY described in Dalla-Vecchia et al. (in preparation) and Schaller et al. (2015b), which uses the pressure-entropy formalism introduced by Hopkins (2013). The

EAGLE subgrid physics model has been calibrated to reproduce the $z = 0.1$ stellar mass function and galaxy sizes in the stellar mass range 10^8–$10^{11} \, \mathrm{M_\odot}$ in a cosmological volume of $100^3 \, \mathrm{Mpc^3}$. It includes radiative metallicity-dependent cooling following Wiersma, Schaye & Smith (2009a), star formation with a pressure-dependent efficiency and a metallicity-dependent density threshold (Schaye & Dalla Vecchia 2008), stellar evolution and stellar mass-loss and thermal feedback that captures the collective effects of stellar winds, radiation pressure and supernova explosions, using the stochastic, thermal prescription of Dalla Vecchia & Schaye (2012). Reionization of hydrogen is assumed to be instantaneous at $z = 11.5$, while He II reionization follows a Gaussian centred at $z = 3.5$ with $\sigma(z) = 0.5$ to reproduce the observed thermal history (Schaye et al. 2000; Wiersma et al. 2009b). The EAGLE model also includes black hole growth fuelled by gas accretion and mergers and feedback from active galactic nuclei (AGN; Booth & Schaye 2009; Johansson, Naab & Burkert 2009; Rosas-Guevara et al. 2015). In this work, we use the 'reference' choice of subgrid parameters (Crain et al. 2015) at all resolutions. Further details of the EAGLE and APOSTLE simulations and comparison of results to observations can be found in the references above.

2.2 Halo and subhalo selection

Structures (haloes) are identified using a Friends-of-Friends algorithm (Davis et al. 1985), and substructures (subhaloes) are identified using the SUBFIND algorithm (Springel et al. 2001, with the extension of Dolag et al. 2009) for 18 snapshots up to a lookback time of 5 Gyr ($z \sim 0.5$). We identify haloes and subhaloes at each snapshot, and find their progenitors at earlier times using a subhalo merger tree (as described in the appendix of Jiang et al. 2014).

We denote the radius inside which the mean density is 200 times the critical density as r_{200}, and the enclosed mass is M_{200}. For substructures, we quote the total mass bound to a subhalo: in the hydrodynamic simulation, this includes dark matter, stellar and gas particles, although in the mass range $10^{6.5}$–$10^{8.5} \, \mathrm{M_\odot}$ we study here, subhaloes are almost entirely devoid of baryons, as reionization has prevented the vast majority from forming stars, and ram pressure stripping has removed any residual gas (Sawala et al. 2016a).

The number of identified subhaloes and the assigned masses depend on the substructure identification algorithm (see Onions et al. 2012 for a comparison). For subhaloes of 10^4 particles, Springel et al. (2008) find that the mass assigned by the SUBFIND algorithm closely follows the mass enclosed within the tidal radius, while Onions et al. (2012) find that substructures can be reliably identified with at least 20 particles and their basic properties can be recovered with at least 100 particles. While the internal structure of subhaloes with so few particles may be affected by numerical effects, their orbits are determined by the structure of the main halo, which is resolved with many more particles. As discussed in Section 3.1, we find that the subhalo mass function converges with resolution in both hydrodynamic and DMO simulations. It should be noted that even if the subhalo mass function is numerically converged, by construction, the SUBFIND mass depends on the local overdensity. Part of the central decline in subhalo number density within a given mass interval is therefore attributable not directly to stripping, but to the increasing background density. However, to first order, as long as the background densities are similar, this should not affect the relative difference in subhalo number density between the DMO and hydrodynamic simulations.
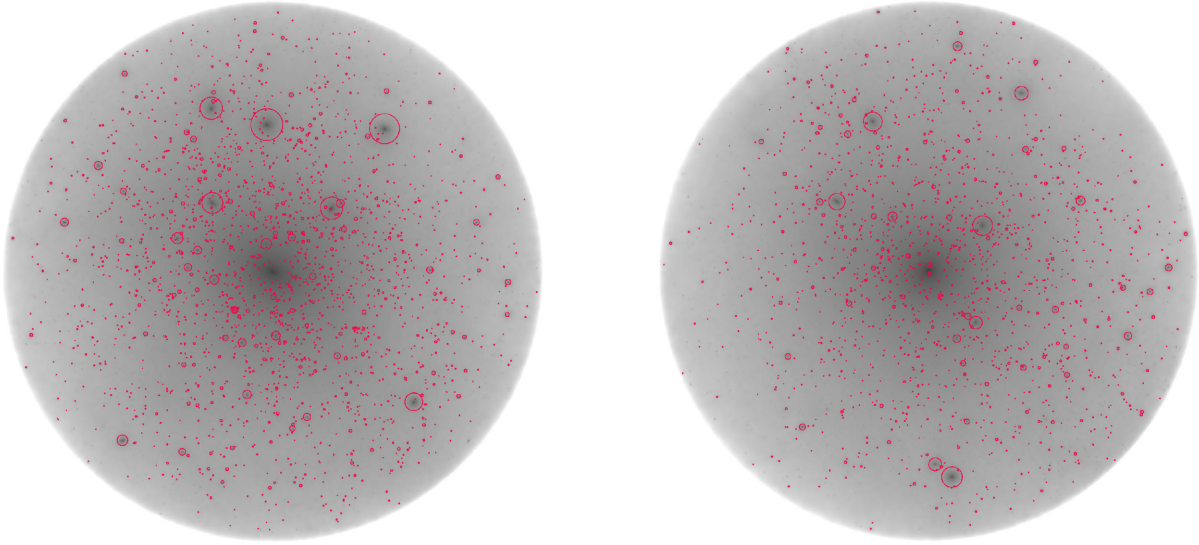
Figure 1. Projected dark matter density at $z = 0$ in the MW-mass halo AP-1-1 at resolution L1, in matched DMO (left) and hydrodynamic (right) simulations inside r_{200}. Red circles indicate the positions of subhaloes with masses above $10^{6.5}$ M$_\odot$ inside the respective regions, with an area proportional to subhalo mass. The hydrodynamic simulation contains fewer subhaloes, and the dark matter in the central region is visibly rounder.

In this work, we limit our analysis to subhaloes with mass above $10^{6.5}$ M$_\odot$, corresponding to at least 50 particles in the L1 DMO simulation. While the potential inside the subhaloes is poorly sampled, their orbits inside the main halo should not be affected. With a gravitational softening length limited to <134 pc at resolution L1, the main haloes are unaffected by softening in the regions of interest here. The dark matter mass profiles of the main haloes and their relation to the disc are discussed further in Schaller et al. (2016).

2.3 Orbits

All three observational probes introduced in Section 1 are sensitive to substructures within the central $\sim$10–20 kpc, equivalent to $\sim$0.05–0.1 $\times$ r_{200} of the host halo at $z = 0$. Throughout this work, we use the minimum of the host halo potential to define the origin of our reference frame, and the minimum of each satellite's potential to define its position.

Our simulation snapshots are spaced equally in $\log(a)$, with a maximum time interval of 33 Myr. Because most subhaloes found near the halo centre at any time have orbits with large apocentres and cross the central regions at a high speed (see Section 4.2), any single snapshot only captures a small fraction of all the subhaloes that come near the halo centre. To obtain a complete measurement of the expected subhalo distribution, we therefore interpolate all orbits using cubic splines, and integrate all quantities over time to determine their expected probability density. Except in Figs 1 and 2, which show results based only on the single snapshot at $z = 0$, throughout the remainder of this paper, we state an expectation value for the number of subhaloes of a certain mass, and its distribution in either real or velocity space. In this way, we can accurately compute the expected subhalo distribution despite the finite time resolution of our simulation snapshots.

Subhalo velocities are commonly measured using a mass-weighted average of the particle velocities, and thus defined relative to the centre-of-mass (CM) frame. However, because the host halo potential can be offset from the CM by $\sim$10 kpc, subhalo

velocities measured in this way cannot be used directly for our purpose. Instead, we establish velocities consistent with our centre-of-potential reference frame from the interpolated positions. Details are described in Appendix A.

Where we average our results over the haloes listed in Table 1, we first compute the properties of subhaloes relative to the individual host halo's properties such as r_{200}, potential, where appropriate, and then combine the results of all orbits from all haloes to compute the arithmetic mean.

3 SUBHALO ABUNDANCE

Fig. 1 illustrates the spatial distribution and the effect of baryons on the number of substructures by comparing the present-day projected mass distribution and the location of substructures with masses above $10^{6.5}$ M$_\odot$ in one of our Milky Way mass haloes in DMO and hydrodynamic simulations (identified as halo AP-1-1 in Table 1). In the DMO simulation, shown on left, the halo has a total mass of $M_{200} = 1.65 \times 10^{12}$ M$_\odot$ and a corresponding $r_{200} = 236$ kpc, reducing slightly to $M_{200} = 1.57 \times 10^{12}$ M$_\odot$ and $r_{200} = 232$ kpc in the hydrodynamic simulation shown on the right. For this particular halo, and at this particular snapshot, a reduction in substructures is barely noticeable by eye, and robust quantitative statements require a more detailed analysis.

3.1 Total subhalo abundance

Fig. 2 shows the cumulative abundance of substructures as a function of subhalo mass, averaging over four MW mass haloes in both DMO and hydrodynamic simulations, at our three resolution levels from L3 (lowest), through L2 (intermediate) to L1 (highest). In the left-hand panel, all subhaloes, both inside and outside r_{200}, are included out to a distance of 300 kpc. As noted in previous works (e.g. Geen et al. 2013; Sawala et al. 2013), for subhaloes of mass $<10^{9.5}$ M$_\odot$, there is a near-constant decrease in abundance by $\sim$1/3 in the hydrodynamic relative to the DMO simulation. In the
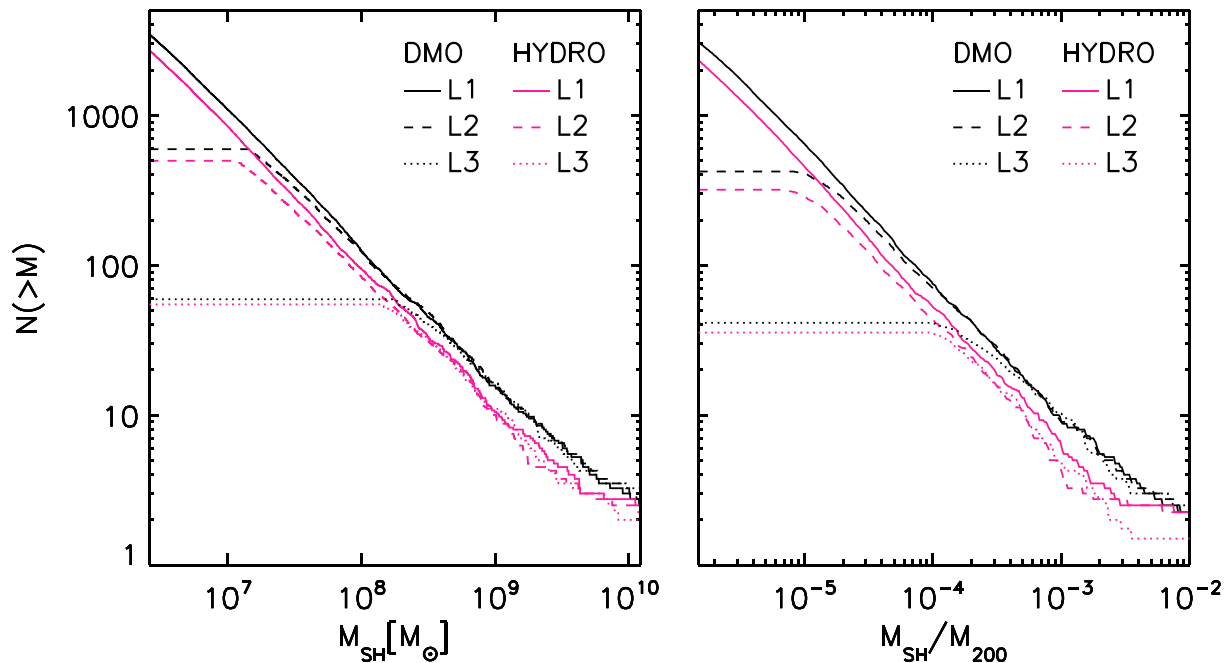
Figure 2. Cumulative abundance of substructures in the Milky Way mass haloes at the present time. Each panel presents results averaged over the four haloes listed in Table 1 simulated as DMO (black lines) or hydrodynamically (red lines), at three different resolutions, from L3 (dotted, lowest), through L2 (dashed, intermediate) to L1 (solid, highest). The left-hand panel shows subhaloes within 300 kpc of each host, while the right-hand panel includes subhaloes within r_{200}, with the mass expressed relative to the hosts' M_{200}. Convergence of the DMO and hydrodynamic simulations is similar, and the relative difference between the hydrodynamic and DMO simulations is similar at different resolution levels.

Table 1. Haloes used in this study.

	DMO		Hydrodynamic		
	M_{200} $[10^{12}\,\mathrm{M_\odot}]$	N_s	M_{200} $[10^{12}\,\mathrm{M_\odot}]$	M_* $[10^{10}\,\mathrm{M_\odot}]$	N_s
AP-1-1	1.65	3720	1.57	2.75	2905
AP-1-2	1.10	3491	1.01	1.20	2648
AP-4-1	1.34	4640	1.16	1.23	3564
AP-4-2	1.39	3270	1.13	1.88	2785

Notes. Structural parameters of the four APOSTLE haloes used in this study at $z = 0$ and resolution L1, in the DMO and hydrodynamic simulations. All values are in physical units. M_{200} is computed for the total halo, including subhaloes, while stellar masses are those of the central galaxy excluding satellites. N_s denotes the number of subhaloes in the mass range $10^{6.5}$–$10^{8.5}\,\mathrm{M_\odot}$ inside r_{200}.

right-hand panel, subhalo masses are expressed relative to the M_{200} of the host, and subhaloes are selected inside the hosts' r_{200}. Although the decrease in abundance in the hydrodynamic simulation is slightly enhanced by the reduction of r_{200}, the principal difference in abundance between the DMO and hydrodynamic simulation persists. Clearly, baryons affect the masses of subhaloes below $10^{9.5}\,\mathrm{M_\odot}$ more than those of their $10^{12}\,\mathrm{M_\odot}$ hosts, destroying the scale-free nature of pure dark matter simulations. On the other hand, below $\sim 10^{9.5}\,\mathrm{M_\odot}$, the offset in the abundance is nearly constant, as the baryon loss of subhaloes in this mass range is nearly constant.

3.2 Baryon effects on subhalo abundance

In Fig. 3, we show the cumulative mass functions of substructures in four spherical shells, increasing in radius, from 0–10 to 10–20, 20–50 and 50–200 kpc. The results are averaged over all four haloes

at resolution L1, and time-averaged in lookback time over either five intervals of 1 Gyr each, or over a 5 Gyr period.

Comparing the results from the hydrodynamic and DMO simulations, it can be seen that, in all shells, the abundance of substructures is reduced in the hydrodynamic simulation. The difference increases with decreasing radius, indicating stronger tidal stripping near the centre in the hydrodynamic simulation.

We fit the subhalo mass functions in all four shells by power laws, $dn/dm \propto m^n$, and overplot the fits as dark grey lines in the large panels of Fig. 3. In both DMO and hydrodynamic simulations, the results are similar to those reported in the AQUARIUS simulations by Springel et al. (2008), who found values between -1.93 and -1.87 for the slope, with the steepest values found for the lowest mass range. We find slightly shallower profiles in the innermost bins, but no significant differences in slope between DMO and hydrodynamic simulations. In the mass range $10^{6.5}$–$10^{8.5}\,\mathrm{M_\odot}$, the depletion of substructures due to the presence of baryonic effects, namely the removal of the gas by reionization and ram-pressure stripping prior to infall and subsequently the enhanced tidal stripping in the steeper potential of the host halo, does not depend on subhalo mass.

In the bottom panels of Fig. 3, we show the ratios between the subhalo abundances in the hydrodynamic and DMO simulations in the different radial shells. We overplot, in dark grey, the ratio between the two respective power-law fits and, in light grey, a fit to a constant value over the entire mass range shown. We find that, in the subhalo mass range $10^{6.5}$–$10^{8.5}\,\mathrm{M_\odot}$, a factor constant in mass that varies only with radius gives an almost equally good fit to the suppression of substructures: by 23 per cent for $r = 50$–200 kpc, 40 per cent for $r = 20$–50 kpc, 45 per cent for $r = 10$–20 kpc, and 48 per cent for $r < 10$ kpc. We list the best-fitting power-law slopes, and the constant reduction factors in Table 2.
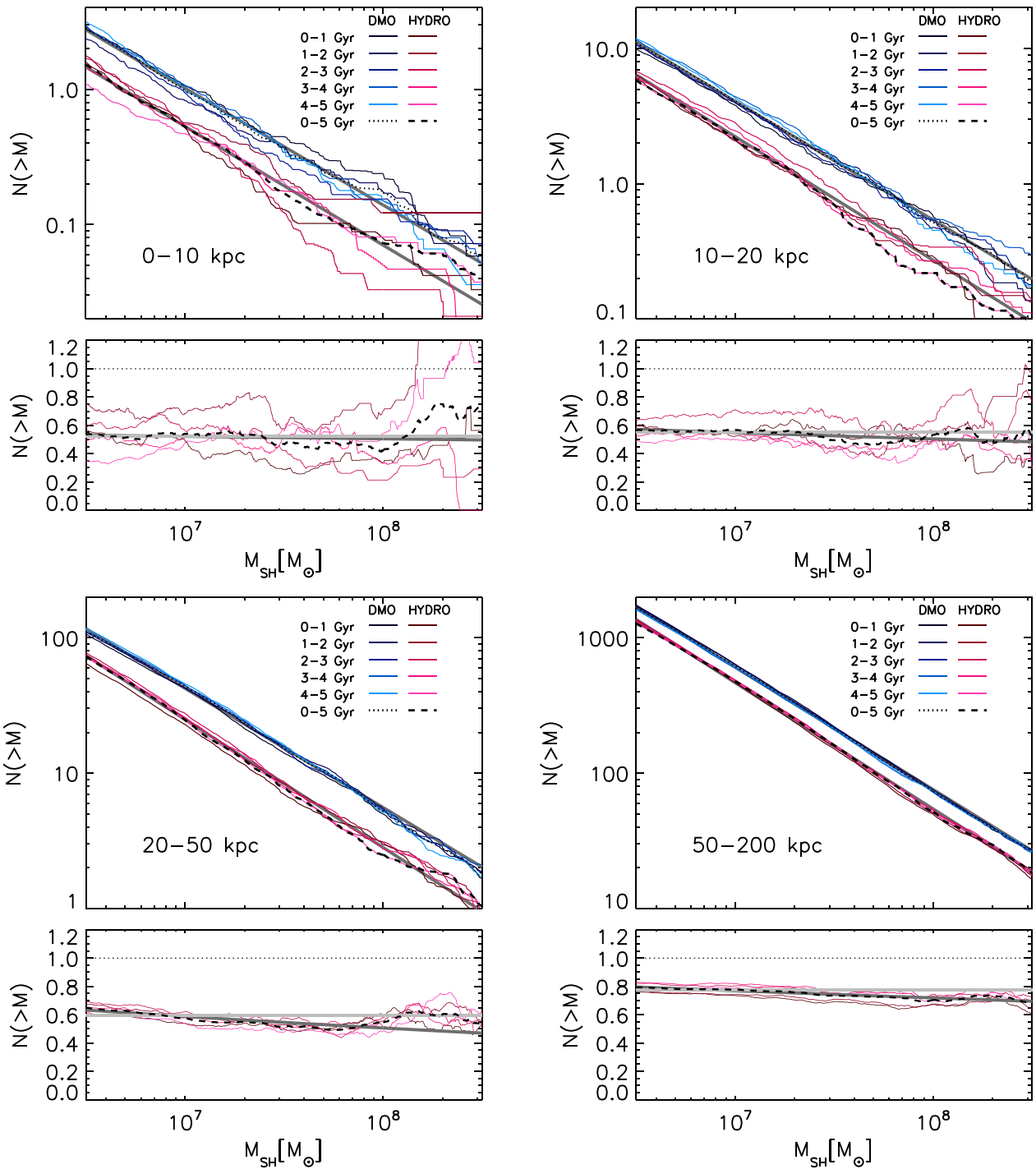
Figure 3. Large panels: cumulative substructure mass functions in spherical shells, in the DMO and hydrodynamic simulations. Blue and red solid lines indicate results from the DMO and hydrodynamic simulations over successive 1 Gyr time intervals, respectively, while dotted and dashed lines show the results averaged over the entire 5 Gyr period. Dark grey lines are power-law fits to the mass functions over the mass interval shown. Small panels: ratio between the cumulative substructure mass functions in the DMO and hydrodynamic simulations. Solid dark grey lines show the ratios between the power-law fits to the DMO and hydrodynamic mass functions, solid light grey lines are constant values. Differences between the hydrodynamic and DMO simulation are present at all radii, but increase towards the centre. For substructures in the range $10^{6.5}$–$10^{8.5}$ $M_\odot$, there is little evidence of a mass or time dependence.

As discussed in Sawala et al. (2013) and Schaller et al. (2015a), the mass-loss of isolated subhaloes due to the complete loss of baryons relative to a DMO simulation is nearly constant below $\sim 10^9$ $M_\odot$, and the reduction in abundance by ~ 23 per cent in the outermost shell is consistent with the re-

sults expected for isolated subhaloes. Note that this does not mean that these subhaloes do not experience tidal stripping, but merely that, at these large radii, there is little difference in tidal stripping between the DMO and hydrodynamic simulations.

Table 2. Subhalo abundance parameters.

	0–10 kpc	10–20 kpc	20–50 kpc	50–200 kpc
	Power-law slope n^a			
DMO	−1.86	−1.88	−1.88	−1.90
Hydro	−1.88	−1.91	−1.94	−1.93
	$N_{\mathrm{Hydr}}(r)/N_{\mathrm{DMO}}(r)^b$			
	0.52	0.55	0.60	0.77

Notes. ^{a}Power-law slopes for the subhalo mass functions in the DMO and hydrodynamic simulation in the mass range $10^{6.5}$–$10^{8.5}$ M$_\odot$.
^{b}Suppression of the number of substructures in the hydrodynamic relative to the DMO simulation, assuming a constant factor, independent of mass.

Figure 4. Top: number density profiles of substructures in the mass range $10^{6.5}$–$10^{8.5}$ M$_\odot$ (dashed lines, left axis) and dark matter mass density profiles (solid lines, right axis). Black and grey lines show results of the DMO and hydrodynamic simulations, respectively, blue and red lines show fits to the two sets of simulation data; dashed for (α, β, γ) fits to the subhalo number densities, solid for NFW fits for the DM mass densities, at $z = 0$. Bottom: expected radial velocity dispersion of subhaloes relative to velocity dispersion of DM particles at $z = 0$ from equation (4) given the above radial density profiles, normalized to the respective values at 300 kpc. Dotted and dashed lines indicate the scale radii of the NFW fit to the particle densities, and of the (α, β, γ) profiles for the subhalo number densities, respectively.

3.3 Substructure and mass profiles

In the top panel of Fig. 4, we compare the mass density profiles of dark matter at $z = 0$ to the number density profiles of subhaloes in the mass range $10^{6.5}$–$10^{8.5}$ M$_\odot$ in our DMO and hydrodynamic simulations, each averaged over four haloes.

We find that the averaged mass density profiles, represented by solid lines, are well described by NFW-profiles (Navarro, Eke & Frenk 1996) of the form

$$\rho(r) = \rho_s \left(\frac{r}{r_s}\right)^{-1}\left(1 + \frac{r}{r_s}\right)^{-2}, \qquad (1)$$

with values for the scale radii, r_s, of 29 kpc and 22 kpc, and densities at the scale radii, ρ_s, of 3.08×10^6 M$_\odot$ kpc^{-3} and $4.58 \times^6$ M$_\odot$ kpc^{-3} for the DMO and hydrodynamic simulations, respectively. As expected, since the total dark matter mass is lower in the hydrodynamic simulations, the average DM density in the haloes is below that of the DMO counterparts. However, due to adiabatic contraction, the DM distribution is more concentrated in the hydrodynamic simulations, and the DM density slightly exceeds that of the DMO simulations near the centre. With the addition of baryons, the total mass density in the hydrodynamic simulations exceeds that of the DMO simulations.

Compared to the DM mass density profiles, the subhalo number density profiles, represented by dashed lines in Fig. 4, are much shallower towards the centre. We fit these by more general, double power-law models (sometimes called α, β, γ- models, e.g. Zhao 1996) of the form

$$\rho(r) = \rho_s \left(\frac{r}{r_s}\right)^{-\gamma}\left(1 + \left(\frac{r}{r_s}\right)^{\alpha}\right)^{(\gamma-\beta)/\alpha}. \qquad (2)$$

Here, α determines the transition between an inner power law with asymptotic slope $-\gamma$ and an outer power law with asymptotic slope $-\beta$, centred on the scale radius r_s, where the density is ρ_s. The two-parameter NFW model (equation 1) is a special case of this five-parameter model for $(\alpha, \beta, \gamma) = (1, 3, 1)$.

For the substructure number density profile in the mass range $10^{6.5}$–$10^{8.5}$ M$_\odot$, averaged over four haloes in each simulation, we obtain best fits of

$$(r_s, \rho_s, \alpha, \beta, \gamma) = (79.5 \text{ kpc}, 1.06 \times 10^{-3} \text{ kpc}^{-3}, 3.06, 0.99, 0.56)$$

and

$$(r_s, \rho_s, \alpha, \beta, \gamma) = (80.7 \text{ kpc}, 2.02 \times 10^{-3} \text{ kpc}^{-3}, 4.82, 0.71, 0.44)$$

for the DMO and hydrodynamic simulations, respectively. Note that because the subhalo mass function does not significantly change with radius, the subhalo number density and subhalo mass density have the same radial dependence.

The most important differences between the subhalo number density profiles and the mass density profiles are the inner slopes, $-\gamma$, and the associated scale radii, r_s. In both DMO and hydrodynamic simulations, the substructure number density profiles transition to much shallower profiles at much greater scale radii than the DM mass density profiles. The difference in inner slope and scale radius between the DMO and hydrodynamic simulations is less significant than recently reported by Zhu et al. (2016). However, these authors also found a mass dependence, and overall, large scatter in the inner log slopes, possibly attributable to the small sample size and required extrapolation. Reflecting the results of Section 3.2, the subhalo number density at a given radius is lower in the hydrodynamic simulations. Consequently, we find that the 'substructure bias' – the relative underdensity of subhaloes compared to DM particles towards the centre, already identified by Ghigna et al. (2000) based on DMO simulations – is even stronger in the hydrodynamic simulations, where the central DM density is higher and the central subhalo density is lower, compared to the DMO counterparts. The outer slope, β, is quite poorly constrained, and the differences are not significant for the central subhalo deficit.

4 SUBHALO VELOCITIES

The disruption of substructures, and the impact of baryons are also reflected in the subhalo velocities. In Section 4.1, we compute the expected velocity bias of subhaloes relative to DM particles. In

Section 4.2, we discuss the distributions of energies and angular momenta, and in Section 4.3, we present the subhalo anisotropy profiles.

4.1 Subhalo velocity bias

For a spherical halo of size R containing populations of particles in equilibrium, assuming isotropy, the radial velocity dispersion, $\sigma_r(r)$, of each population is related to its density, $\rho(r)$, (e.g. Binney & Tremaine 2008), via

$$\rho(r)\sigma_r^2(r) - \rho(R)\sigma_r^2(R) = \int_r^R \rho(r)\frac{GM(r)}{r^2}\mathrm{d}r, \quad (3)$$

where $M(r)$ is the enclosed mass. For $r \ll R$, $\rho(R) \ll \rho(r)$ and the second term on the LHS can be ignored. Using the results for the substructure density profiles for both DM particles and subhaloes in Section 3.3, as suggested by Diemand, Moore & Stadel (2004), we can thus calculate the expected velocity bias of the subhaloes relative to the DM particles.

$$\frac{\sigma_{r,\mathrm{sub}}(r)}{\sigma_{r,\mathrm{DM}}(r)} = \left(\frac{\rho_{\mathrm{DM}}(r)}{\rho_{\mathrm{sub}}(r)} \frac{\int_r^R \rho_{\mathrm{sub}}(r)\frac{M(r)}{r^2}\mathrm{d}r}{\int_r^R \rho_{\mathrm{DM}}(r)\frac{M(r)}{r^2}\mathrm{d}r} \right)^{1/2}. \quad (4)$$

With the parametrization for $\rho_{\mathrm{DM}}(r)$ and $\rho_{\mathrm{sub}}(r)$ given by equations (1 and 2), respectively, and assuming that the velocity bias vanishes beyond $=300$ kpc, where the subhalo number density and DM mass density are small and the majority of subhaloes have not been affected by stripping, we can compute the expected velocity bias of subhaloes relative to DM particles.

The expected velocity biases for the DMO and hydrodynamic simulations are shown in the bottom panel of Fig. 4. It can be seen that for both simulations, the velocity bias rises towards the centre, most steeply between the (larger) scale radius of the (α, β, γ) subhaloes number density profiles and the (smaller) scale radius of the (NFW) DM density profiles, where the difference between the two slopes is maximal. Because of the stronger substructure bias, the expected velocity bias is likewise stronger in the hydrodynamic simulation.

4.2 Orbital energy and angular momentum

Assuming spherical symmetry about the centre of potential and truncation at r_{200}, we compute the halo potential $\Phi(r)$ from the density $\rho(r)$ of all particles at each snapshot:

$$\Phi(r) = -4\pi G \left(\frac{1}{r}\int_0^r \rho(r')r'^2\mathrm{d}r' + \int_r^{r_{200}} \rho(r')r'\mathrm{d}r' \right)$$

In Fig. 5, we show the three 2D density distributions[1] of specific orbital energies, specific orbital angular momenta and radii, of subhaloes in the mass range $10^{6.5}$–$10^{8.5}$ M$_\odot$ inside r_{200} from orbits interpolated over 5 Gyr in lookback time. We normalize the energies, E, by the total energy of a circular orbit at r_{200}, $E_{\mathrm{circ, 200}}$, the angular momenta, L, by the angular momentum of a circular orbit of the same energy, $L_{\mathrm{circ}}(E)$, and the radius r by the virial radius, r_{200}.

---

[1] In Figs 5 and 7 we use the interpolated orbits of all subhaloes in the mass range $10^{6.5}$–$10^{8.5}$ and within the specified radii and time intervals to construct time-averaged 2D histograms. The histograms are normalized by the maximum occupation value for each pair of otherwise identical DMO and hydrodynamic panels, and coloured using the linear colour scales, where 0 is an occupation of 0, and 1 is the maximum occupation, as indicated by the colour bars to the right of both figures.

Note that since our potential definition has the zero-point at infinity (neglecting all mass beyond r_{200}), the total energy of a circular orbit at r_{200} is negative. As a result, subhalo orbits that are more bound, corresponding to more negative total energies, have higher values of $E/E_{\mathrm{circ, 200}}$.

The left column of Fig. 5 shows the E–L probability density. Because the energy of a circular orbit increases monotonically with radius, subhaloes close to $L/L_{\mathrm{circ}}(E) = 1$ are ordered by radius: those located at r_{200} are located at $(L/L_{\mathrm{circ}}(E), E/E_{\mathrm{circ, 200}}) = (1, 1)$. Circular orbits with smaller radii have more negative energies, and line up above this point.

In the middle and right columns of Fig. 5, we show the distributions of $L/L_{\mathrm{circ}}(E)$ and $E/E_{\mathrm{circ, 200}}$, respectively, both versus r/r_{200}. In the L–R plane, we see that the average circularity increases slightly from r_{200} to $\sim 0.2 r_{200}$ (corresponding to ~ 50 kpc), as decaying orbits become more circular. By contrast, it declines sharply for smaller radii, indicating a transition towards almost purely radial orbits close to the centre. In the E–R plane, we see that the average specific orbital energy becomes more negative towards the centre, but peaks at $\sim 0.1 r_{200}$ (corresponding to ~ 25 kpc), where the increase in the average kinetic energy of subhaloes compensates for the continuously more negative potential energy. Because the average circularity also declines towards the centre, the increase in kinetic energy indicates an increase in radial velocities of subhaloes at small radii. This effect is slightly stronger in the hydrodynamic simulations.

Since the minimum total energy of a subhalo is given by the potential energy at its radius, the value of $E/E_{\mathrm{circ, 200}}$ is limited from above, explaining the 'forbidden' region for high values of $E/E_{\mathrm{circ, 200}}$ in the E–R plane, seen in the right column of Fig. 5.

For guidance, on the E–L and E–R planes in Fig. 5, the dashed and dotted lines indicate values of $E/E_{\mathrm{circ, 200}} = 1$ and $E/E_{\mathrm{circ, 200}} = 2$, respectively. For orbital energies less negative than $E_{\mathrm{circ, 200}}$, the radius of a circular orbit lies outside r_{200}. For each value of $0 < E/E_{circ, 200} < 1$, there is a maximum circularity for orbits with pericentres inside r_{200}. This explains the 'forbidden' region for high circularities at $E/E_{\mathrm{circ, 200}} < 1$ on the E–L plane. Likewise, a value of $E/E_{\mathrm{circ, 200}} = 2$ is equal to the potential energy at r_{200} and hence the maximum orbital energy for a subhalo on a radial orbit with an apocentre inside r_{200}. Subhaloes on radial orbits with higher energies (values of $E/E_{\mathrm{circ, 200}} < 2$) spend a fraction of their orbital period outside r_{200}, raising the average circularity measured inside r_{200}.

By contrast, the nearly empty region at high values of $E/E_{\mathrm{circ, 200}}$ and low values of $L/L_{\mathrm{circ}}(E)$ in the E–L plane is not a forbidden region. Instead, it reflects the fact that subhaloes with low orbital energies and correspondingly short orbital periods are more easily disrupted on radial orbits. As can be seen by the solid black line on this panel, the median circularity increases for more closely bound subhaloes above $E/E_{\mathrm{circ, 200}} = 2$.

While the subhaloes with the most negative energies thus typically have high circularities and exist only near the halo centre, it does *not* follow that subhaloes near the centre have high circularities: instead, as can be seen on the L–R plane in the middle column of Fig. 5, the average circularity for subhaloes is lowest near the halo centre. Among the subhaloes on orbits with highly negative energies and short orbital periods, subhaloes on more radial orbits get most easily disrupted. However, all subhaloes with short orbital periods are prone to tidal disruption, so the central region of the halo is predominantly populated by high-velocity subhaloes with long orbital periods on highly radial orbits.
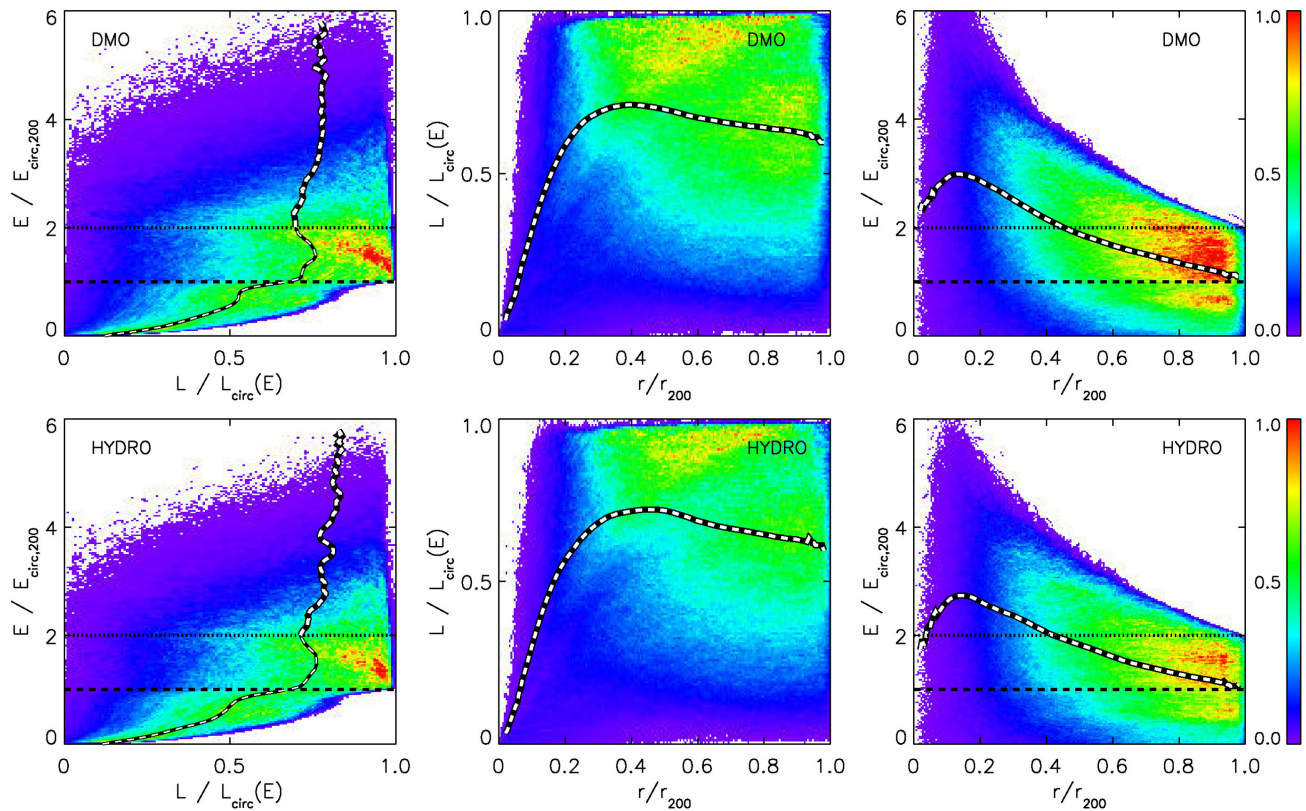
Figure 5. Left: subhalo orbital angular momentum, normalized by the angular momentum of a circular orbit of the same energy, versus subhalo energy, normalized by the energy of a circular orbit at r_{200}. Middle: subhalo distance from the centre normalized by r_{200}, versus normalized angular momentum. Right: normalized subhalo distance versus normalized energy. Note that because the total energy of a circular orbit at r_{200} is negative, bound haloes appear with positive normalized energies. The top row shows results for the DMO simulations, the bottom row shows results for the hydrodynamic simulations. On the left-hand and right-hand panels, the dashed and dotted lines at $E/E_{\mathrm{circ},200} = 1$ and 2 indicate the energy for a halo on a circular orbit at r_{200}, and the potential energy for a halo at r_{200}, respectively. Overplotted on to the left-hand panel is the median of $L/L_{\mathrm{circ}}(E)$ as a function of $E/E_{\mathrm{circ},200}$, overplotted on the middle and right-hand panels are the median of $L/L_{\mathrm{circ},200}$ and $E/E_{\mathrm{circ},200}$, both as a function of r/r_{200}. As explained in Section 4.2, $E/E_{\mathrm{circ},200} < 2$ excludes sections of more radial orbits, while $E/E_{\mathrm{circ},200} < 1$ excludes a fraction of more circular orbits. We indicate this by the thinner line segment on the left-hand panels. See footnote on page 19 for details of the 2D histograms.

4.3 Velocity anisotropy profiles

The velocity anisotropy, $\beta(r)$, quantifies the measured ratio between the kinetic energy due to motions in the radial direction, v_r, and in the tangential direction, $v_t = \sqrt{v_\theta^2 + v_\phi^2}$:

$$\beta(r) = 1 - \frac{\overline{v_t^2(r)}}{2\,\overline{v_r^2(r)}}. \tag{5}$$

Because v_r, v_θ and v_ϕ are three orthogonal velocity components, the velocity anisotropy is zero for equal velocity dispersion in each dimension, positive for more radial orbits and negative for more circular ones.

In the top panel of Fig. 6, we show the velocity anisotropy parameter of subhaloes as a function of radius in our simulations. We find that the velocity anisotropy for subhaloes in the mass range $10^{6.5}$–$10^{8.5}\,\mathrm{M}_\odot$ is close to zero at $r > 50$ kpc in both DMO and hydrodynamic simulations. At smaller radii, the anisotropy rises to $\sim$0.5 near the halo centre. In the bottom panel of Fig. 6, we show the mean of the square of the tangential velocity components, $\overline{v_t^2}$, (dotted lines), and twice the mean of the squares of the radial velocity components, $2\overline{v_r^2}$, (dashed lines), as a function of radius. Both sets of lines rise towards the centre, and are nearly equal at $r > 50$ kpc, corresponding to near-zero velocity anisotropy. At

smaller radii, the average radial velocities rise much more steeply, reflecting the prediction of a centrally rising velocity bias described in Section 4.1. However, the increase in subhalo radial velocities is less than predicted by the spherical equilibrium model, partly due to the fact that subhalo disruption and infall are continuous processes, and the instantaneous velocities of the existing subhaloes are not fully reflective of the difference in the instantaneous substructure bias.

Interestingly, the centrally rising velocity anisotropy for subhaloes is the opposite of that seen for spherical systems composed of indissoluble bodies, such as stars in globular clusters, where orbits become more isotropic near the centre (Osipkov 1979; Merritt 1985). This is easily understood: while interactions isotropize the orbits near the centres of star clusters (e.g. Baumgardt, Hut & Heggie 2002), tidal processes experienced by subhaloes near the centre of a DM halo also lead to their disruption over time. Hence, close to the halo centre, the subhalo population is dominated by subhaloes with small pericentres but much larger apocentres, which limits the work done by tidal forces. As most circular orbits with small pericentres are destroyed, and circular orbits with large pericentres never enter the halo centre, the innermost region contains predominantly subhaloes on highly eccentric orbits, resulting in the increased central velocity anisotropy.
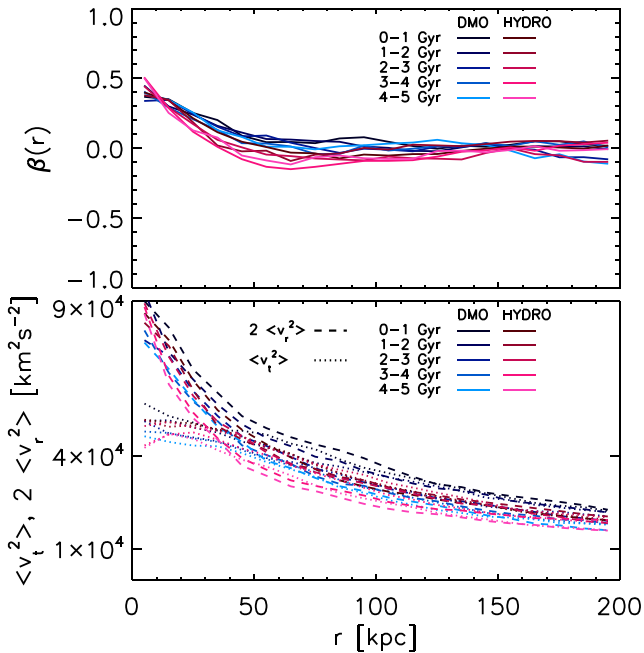
Figure 6. Top: velocity anisotropy parameter, $\beta(r)$, profiles for subhaloes of mass $10^{6.5}$–$10^{8.5}$ M$_\odot$ in the DMO (blue) and hydrodynamic (red) simulations. Bottom: profiles of $2\overline{v_r^2}$ (dashed) and $\overline{v_t^2}$ (dotted) in the same simulations. At large radii, the velocity dispersion in each dimension is similar, and the velocity anisotropy is close to zero. At small radii, there are fewer subhaloes with small radial velocities, and the velocity anisotropy increases.

5 SUBHALO VELOCITY DISTRIBUTIONS

Due to the mass–velocity degeneracy inherent in gravitational interactions of substructures with streams mentioned in the Introduction, the velocity probability density function (VPDF) of substructures is an important prediction of any cosmological model. In this section, we revisit the common assumption of locally Maxwellian velocity distributions, and show that it is increasingly violated towards the halo centre. We propose instead to parametrize the radial velocity, v_r, by a bimodal Gaussian, and composites such as the tangential velocity, v_t, and the total velocity norm, $|v|$, by Rician distributions. We emphasize that such simple, analytical parametrizations are necessarily simplistic descriptions of the data, and should not be expected to precisely capture the full VPDF in the presence of complex physical phenomena.

5.1 Non-Maxwellian distributions

The velocity distribution of particles in haloes is commonly characterized by a (locally) Maxwellian VPDF. A Maxwellian VPDF arises under the assumption that particle velocities are isotropic, such that all three velocity components are independent random variables whose probability density functions (PDFs) are each given by normal distributions,

$$P(v_i) = \frac{1}{\sigma\sqrt{2\pi}}e^{-\frac{v_i^2}{2\sigma^2}},\tag{6}$$

where σ is the velocity dispersion in one dimension, and isotropy implies a mean velocity of zero. If the three components are in-

dependent and have identical distributions, integration over one or two variables yields the 2D or 3D Maxwellian velocity PDFs,

$$P(|v_{2D}|) = \frac{v}{\sigma^2}e^{-v^2/(2\sigma^2)},\tag{7}$$

also called the Rayleigh distribution, and

$$P(|v_{3D}|) = \sqrt{\frac{2}{\pi}}\frac{v^2}{\sigma^3}e^{-v^2/(2\sigma^2)},\tag{8}$$

which is known as the Maxwell–Boltzmann distribution.

If v_r, v_θ and v_ϕ are independent degrees of freedom with equal Gaussian distribution functions, the tangential velocity, v_t, should follow equation (7), and the norm of the total velocity, $|v| = \sqrt{v_r^2 + v_t^2}$, should follow equation (8).

While a local Maxwellian is a simple way to parametrize the total velocity distribution, Kazantzidis, Magorrian & Moore (2004) have shown that it is in fact not a steady-state solution to the velocity distribution inside NFW haloes, as it leads to a quick dissolution of the cusp. It has also been noted that a Maxwellian distribution is not a good fit to the particle velocities measured in a high-resolution numerical simulations, and Vogelsberger et al. (2009) have shown that DM particles have prominent and long-lived, non-Gaussian velocity substructures that are relics of the assembly history of the halo. Vergados, Hansen & Host (2008) argued that the particle velocity distribution in an NFW-like halo should follow a Tsallis shape, based on generalized Gaussian distributions that give better fits to the high-velocity tails observed in the central regions of numerical simulations.

Other attempts include truncating the Maxwellian at the escape velocity (see e.g. Fairbairn & Schwetz 2009), while Kuhlen et al. (2010) opted empirically to fit more general distribution functions of the form:

$$f(v_r) = \frac{1}{N_r}e^{-(v_r^2/2\sigma_r^2)^{\alpha_r}}, \quad f(v_t) = \frac{v_t}{N_t}e^{-(v_t^2/2\sigma_t^2)^{\alpha_t}},\tag{9}$$

where N_t and N_r are normalization constants, and α_r and α_t generalize the 1D and 2D Maxwellian distributions by including additional free parameters.

Independent of the velocity distributions for *particles*, it is worth noting that the velocity profile of substructures may be substantially different (see Section 4.1). As we discuss below, we also find the Maxwellian velocity distribution to be merely a limiting case, only approximately true at large radii and low velocities. It is strongly violated near the centre, where the velocity anisotropy and the preferential disruption of low-velocity subhaloes leads to highly non-Gaussian and non-Maxwellian VPDFs.

5.2 Total velocities

The specific kinetic energy of a subhalo equals $\frac{1}{2}|v|^2 = \frac{1}{2}(v_t^2 + v_r^2)$, where v_r and v_t are the radial and tangential velocities. However, while there is considerable scatter in the specific kinetic energies of different subhaloes at each radius, v_r and v_t of a subhalo are clearly not independent.

Instead, near the halo centre, the radial and tangential velocities of subhaloes have a bivariate velocity distribution, whose maximum occurs at some distance $\mu > 0$ from the origin, with very few low-velocity subhaloes. Instead of a Maxwellian, the PDF for $|v| = \sqrt{v_t^2 + v_r^2}$ may be described by a Rician (Rice 1945):

$$P(|v|) = \frac{|v|}{\sigma^2}e^{\frac{-(|v|^2+\mu^2)}{2\sigma^2}}I_0\left(\frac{|v|\mu}{\sigma^2}\right),\tag{10}$$
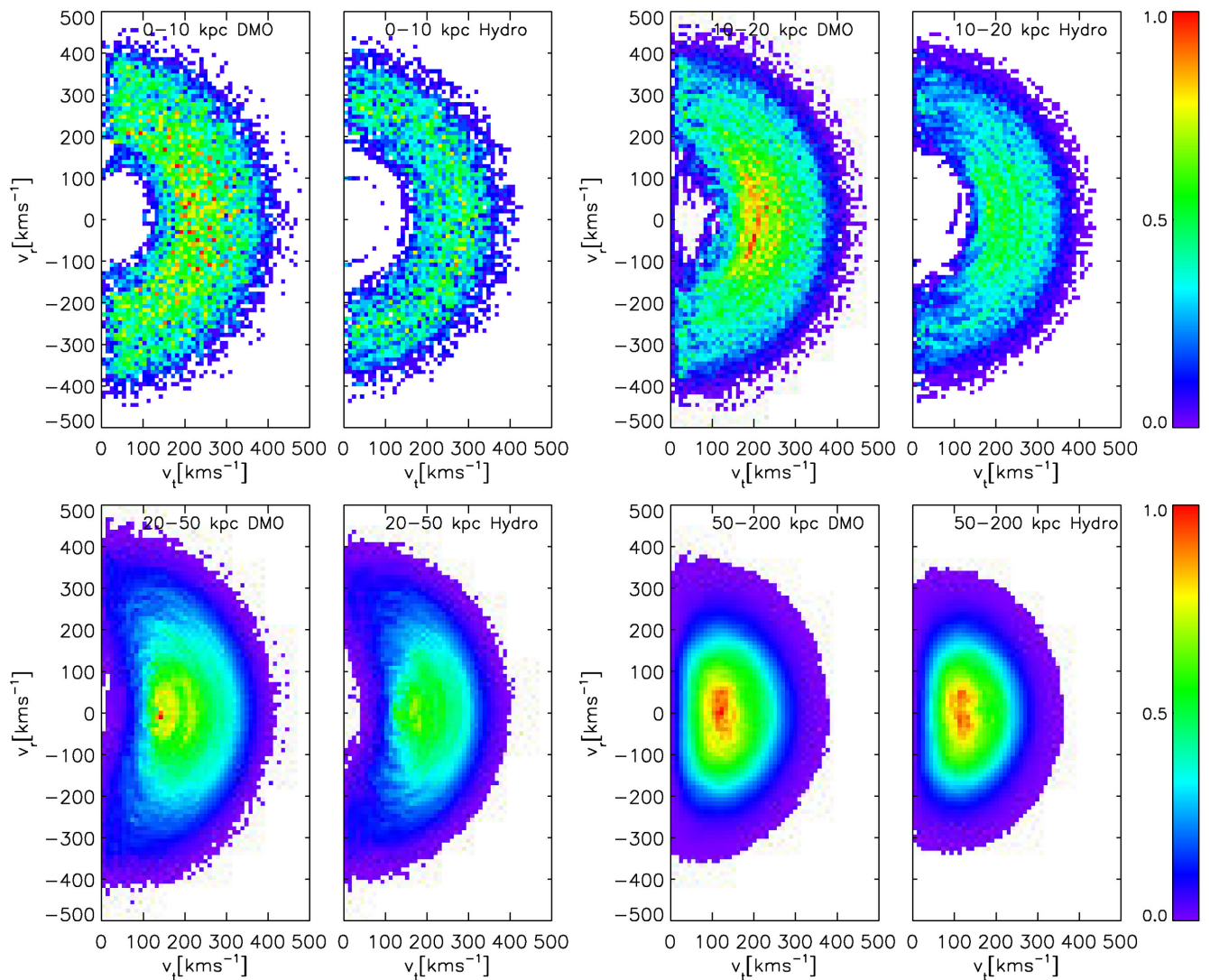
Figure 7. Subhalo velocity distributions in the $v_r - v_t$ plane, in different radial shells, and for the DMO and hydrodynamic simulations, using all four haloes over 5 Gyr lookback time. At small radii, v_r and v_t are highly correlated, such that the mean velocity, $|v| = \sqrt{v_r^2 + v_t^2}$ is approximately constant. At large radii, the mean velocity $|v|$ is smaller, so v_t and v_r are more independent, approximating a 2D Maxwell distribution. It can also be seen that, at all radii, the velocity distribution is slightly more concentrated in the hydrodynamic simulations, which is also evident from the projected velocity distributions shown in Fig. 8. See footnote on page 19 for details of the 2D histograms.

where I_0 is the zeroth-order modified Bessel function of the first kind.

The discrepancy from a Maxwellian (equation 8) is maximal at small radii, where the mean specific kinetic energy is maximal, and decreases as the mean specific kinetic energy decreases at large radii. In the limit of $\mu = 0$, v_t and v_r become independent, $I_0(0) = 1$, and the velocity distribution approaches a 2D-Maxwellian.

Fig. 7 demonstrates this behaviour in our simulations. It shows the 2D velocity distribution function in the (v_r, v_t)-plane measured over 5 Gyr in four radial bins, increasing in radius from top left to bottom right. At $r < 10$ kpc, μ exceeds the scatter, σ, reflecting the near-absence of slow-moving subhaloes with low values of both v_r and v_t. At larger radii, the average kinetic energy decreases and becomes comparable to the scatter. Here, the velocity components v_r and v_t become more independent, except for extreme values, where

the orbital speed is limited by the escape speed, ~350–$400\,\mathrm{km\,s^{-1}}$ at 50 kpc.

In the left column of Fig. 8, we show the PDFs of $|v|$ in the DMO and hydrodynamic simulations in the same four radial bins shown in Fig. 7, together with fits to the Rician PDFs (equation 10). We list the values of μ and σ in Table 3. As expected, we find μ to increase towards the centre, from 165 and $162\,\mathrm{km\,s^{-1}}$ at $50-200$ kpc, to 284 and $290\,\mathrm{km\,s^{-1}}$ at <10 kpc, for the DMO and hydrodynamic simulations, respectively. The scatter σ is less dependent on radius, but it is ~10–$20\,\mathrm{per\,cent}$ lower in the hydrodynamic simulations compared to the DMO simulations.

For comparison, in Appendix B, we contrast Rician and Maxwellian fits to the data shown in Fig. 8. We find that the latter fits are very poor near the halo centre, but that the distributions become more similar at the largest radii, as expected.
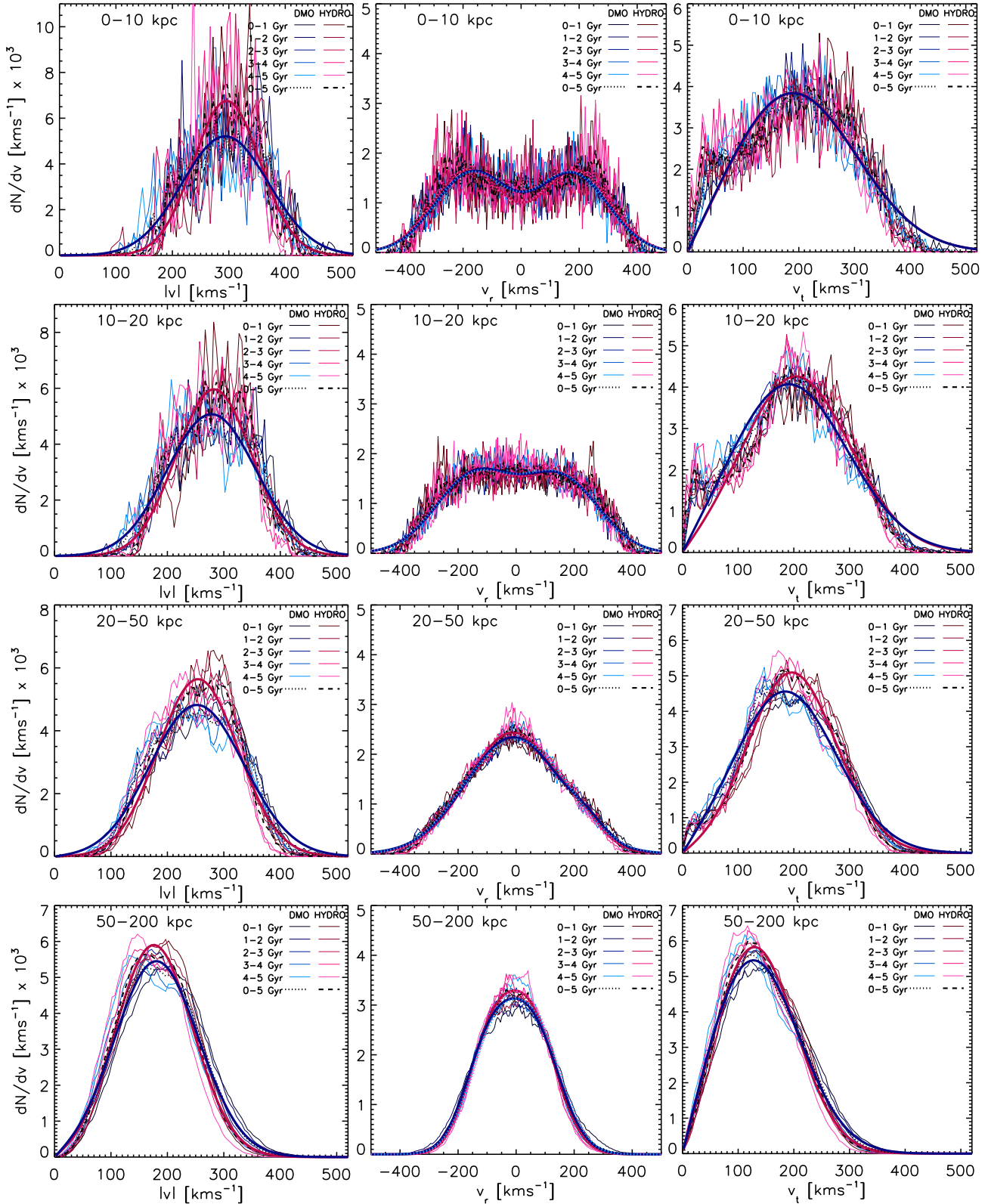
Figure 8. PDFs of subhalo velocities and velocity components in four radial shells for the same haloes and subhaloes shown in Fig. 3. On all panels, thin lines show the results during different lookback time intervals; dotted and dashed black lines show the time-averaged results in the DMO and hydrodynamic simulations. Thick coloured lines show analytical fits, as described below. Left column: total velocity, $|v|$, with Rician fits (equation 10, solid lines). Middle column: radial velocity, v_r, with fits to a general double-Gaussian with five free parameters (equation 11, solid lines) and to a symmetric double-Gaussian with two free parameters (equation 12, dotted lines). Right column: tangential velocity, v_t, with Rician fits (equation 10, solid lines). Note that the difference between individual time intervals is typically less than the scatter. A clear comparison between the time-averaged values and the fits is also shown in Fig. B1.

Table 3. Subhalo velocity PDF parameters.

	0–10 kpc	10–20 kpc	20–50 kpc	50–200 kpc
	v_r PDF parameters μ, σ [kms^{-1}]^a			
DMO	173.3, 125.4	149.1, 131.0	91.3, 141.1	75.6, 88.7
Hydro	188.0, 120.7	151.6, 128.7	89.1, 134.2	71.7, 85.1
	v_t PDF parameters μ, σ [kms-1]^b			
DMO	159.3, 119.2	165.3, 109.2	163.1, 95.1	104.6, 86.2
Hydro	161.6, 118.4	181.4, 101.0	180.2, 82.4	110.3, 77.3
	$|v|$ PDF parameters μ, σ [kms^{-1}]^b			
DMO	283.5, 78.0	266.6, 80.4	238.4, 85.4	165.0, 77.2
Hydro	290.3, 59.7	274.5, 67.9	244.1, 72.6	162.5, 70.8

Notes. ^{a}For a symmetric double-Gaussian VPDF, as in equation (12).
^{b}For a Rician VPDF, as in equation (10).

5.3 Radial velocities

As noted in Section 4.2, the subhalo population near the centre is dominated by subhaloes on radial orbits with long orbital periods. Consequently, for small radii, the radial velocity distribution of subhaloes is described by a double-peaked Gaussian of the general form:

$$P(v_r) = \frac{a}{\sigma_1\sqrt{2\pi}}e^{-\frac{(v_r-\mu_1)^2}{2\sigma_1^2}} + \frac{1-a}{\sigma_2\sqrt{2\pi}}e^{-\frac{(v_r-\mu_2)^2}{2\sigma_2^2}} \quad (11)$$

where the five free parameters μ_1, μ_2, σ_1, σ_2 and a represent the mean and standard deviations of the first and second Gaussian components, as well as the relative contribution of the two components. A double Gaussian models the subhalo population at each radius as a sum of an 'incoming' and an 'outgoing' population. In the full, five-parameter fit, we typically find a small negative mean radial velocity, indicating either more incoming than outgoing satellites as a result of recent infall and disruption, or satellites losing orbital energy as a result of dynamical friction. However, if orbital energy is exactly conserved, equation (11) can be simplified to a symmetric double-Gaussian, where we set $\sigma = \sigma_1 = \sigma_2$, $\mu = \mu_1 = -\mu_2$ and $a = (1-a) = 1/2$:

$$P(v_r) = \frac{1}{2\sigma\sqrt{2\pi}}e^{-\frac{(v_r-\mu)^2}{2\sigma^2}} + \frac{1}{2\sigma\sqrt{2\pi}}e^{-\frac{(v_r+\mu)^2}{2\sigma^2}} \quad (12)$$

The middle column of Fig. 8 shows fits to our simulation data using both equations (11 and 12), and we list the best-fitting values for μ and σ for both DMO and hydrodynamic simulations in Table 3. It can be seen that, at large radii, $\sigma > \mu$, resembling a (broadened) peak centred at $v_r = 0$, approaching a single Gaussian in the limit $\mu = 0$. At smaller radii, μ increases and the radial velocity distribution becomes increasingly broad and, for $r < 20$ kpc, clearly bimodal. Appendix B compares the bimodal fit to one with a single Gaussian and shows the convergence at large radii.

5.4 Tangential velocities

In principle, there are two orthogonal velocity components, v_θ and v_ϕ, required in addition to the radial velocity, v_r, to fully describe the velocity of a subhalo. Defining the tangential velocity, $v_t = \sqrt{v_\theta^2 + v_\phi^2}$, if its two components are independent Gaussian random variables with zero mean, the PDF for v_t may be expected to be a 2D-Maxwellian (equation 7). At large radii, where the orbital anisotropy is close to zero, we find a relatively good agreement, except for an overprediction at the high-velocity tail, corresponding to subhaloes above the escape velocity. However, as the anisotropy

increases towards the centre, the 2D-Maxwellian shape overpredicts the skewness of the measured v_t distribution. As shown in the right column of Fig. 8, we find that the tangential velocities in each radial bin are quite well fit by Rician distributions (equation 10). In the two innermost shells, there is however a small excess of low-tangential velocities compared to the analytic fits. Appendix B compares the Rician fits to those of a 2D-Maxwellian, which severely overpredict either the high- or low-velocity tails of the distributions at small radii.

6 IMPLICATIONS FOR SUBSTRUCTURE DETECTION

6.1 Substructure detection via lensing

The detection of substructure around individual galaxies by strong gravitational lensing depends not only on the mass of the substructure, but in addition on its projected distance from the Einstein radius. Recently dark substructures have been detected around massive elliptical galaxies that are typically embedded in dark matter haloes, with total masses of $M \sim 10^{13}$ M$_\odot$ and typical Einstein radii of $r_E \sim 10$ kpc (e.g. Vegetti et al. 2012; Nierenberg et al. 2014; Hezaveh et al. 2016). These lensing haloes are an order of magnitude more massive than the Milky Way like host haloes we have studied in this paper.

The substructure abundance clearly depends on the host halo mass and concentration. However, we believe that, when scaled by r/r_{200}, the baryonic effects that suppress substructures found in the APOSTLE simulations are likely to be a reasonable approximation to the effects in host haloes of slightly larger mass, which are expected to have slightly lower halo concentrations and stellar mass fractions (e.g. Moster et al. 2010; Dutton & Treu 2014). While it has been suggested that baryons may significantly affect the subhalo lensing signal (e.g. Macciò et al. 2006), our results indicate that baryonic effects should not be a major obstacle for detecting ΛCDM substructures through lensing, or for ruling out ΛCDM in case of a significant shortfall of detections relative to DMO predictions, at least in haloes with similar central stellar densities and similar amounts of adiabatic contraction.

6.2 Substructure detection via stream gaps

In order to detect dark matter substructures through the perturbations they induce on globular cluster streams, both mass function and the velocity distribution of substructures are important, as the interaction strength is proportional to the mass, and inversely proportional to the relative velocity.

The Milky Way's two most prominent globular cluster streams are Pal-5 and GD-1, both discovered in the SDSS. Pal-5 (Odenkirchen et al. 2001) extends over more than 20°, with apogalactic and perigalactic distances of 18.67 kpc and 7.97 kpc (Küpper et al. 2015), while GD-1 (Grillmair & Dionatos 2006) extends over 63°, with apogalactic and perigalactic distances of 28.75 ± 2 kpc and 14.43 ± 0.5 kpc (Willett et al. 2009). For the observable parts of the Pal-5 stream, Küpper et al. (2015) estimate an age of $3.4^{+0.5}_{-0.3}$ Gyr, while Carlberg & Grillmair (2013) estimate a dynamical age of 2.3–4.6 Gyr for GD-1.

We expect the abundance of substructures inside the orbit of Pal-5 and GD-1 to be reduced by ∼45–50 per cent relative to that inferred from DMO simulations due to baryonic effects, with a slightly larger reduction for Pal-5, due to its smaller mean galactocentric distance.

Compared to earlier work, we find two additional effects that should be taken into account in future work. Erkal & Belokurov (2015b) assume a prior for the substructure mass that is uniform in $\log(M)$, or a mass function with a slope of -1, we find steeper power laws, with slopes between -1.86 and -1.91 in both the DMO and hydrodynamic simulations.

More importantly, it has so far been assumed that the velocity PDF of substructures is Maxwellian, with a mean velocity equal to $v_{circ}/\sqrt{3} = 97\,km\,s^{-1}$ in the case of Erkal & Belokurov (2015b). However, as discussed in Section 5.2, we find that this is a poor fit to the subhalo velocities near the centre, where subhaloes are biased towards much higher velocities, and where the Rician PDF contains far fewer low-velocity subhaloes than a Maxwellian distribution fit to the same data. Comparing the Maxwellian and Rician fits to the total velocity within 10 kpc, shown in Appendix B, we find that the Maxwellians vastly overpredict the number of subhaloes with low velocities, even considering that our Maxwellian fits have mean velocities that are nearly twice as high as those assumed previously. Given that low-velocity perturbers cause larger gaps and are easier to detect, using accurate velocity priors is important for the characterization of perturbers, and any inferences derived from it. An additional effect, particularly relevant for Pal-5, is the potential confusion of perturbations by substructures with those induced by giant molecular clouds. These are, of course, relatively slow moving, and Amorisco et al. (2016) point out that they induce perturbations similar to those caused by dark matter subhaloes.

6.3 Substructure detection via disc heating

Similar to the perturbation of streams, perturbations of the Galactic disc component by substructures are not only sensitive to the substructure mass, but also to their impact velocity. Impacts of dark substructures will heat the disc increasing the vertical velocity dispersion, with the most pronounced effects typically seen in the outer parts of the disc where the lower surface density results in a correspondingly lower restoring force (e.g. Binney & Tremaine 2008). Based on our analysis we find a reduction in the abundance of substructures within 10 kpc of the halo centre by up to a factor of 2 in hydrodynamic simulations compared to DMO simulations. As for stream gaps, the velocity of perturbers determines their interaction strength, and near the centre, we find a much lower number of low-velocity substructures compared to the commonly assumed Maxwellian velocity distribution function.

However, as a caveat it should be noted that the disc may not be such a clean tracer of dark substructures. While Feldmann & Spolyar (2015) estimate perturbations on the order of 1–$2\,km\,s^{-1}$ from a $10^9\,M_{\odot}$ substructure at $400\,km\,s^{-1}$, other massive perturbers such as globular clusters (estimated to contribute $5.5\,km\,s^{-1}$ to the velocity dispersion, Vande Putte, Cropper & Ferreras 2009), or molecular clouds (e.g. Lacey 1984; Hänninen & Flynn 2002) also result in disc heating.

In addition internal mechanisms such as the growth of a central bar component and spiral features in the Galactic disc will also heat the disc (e.g. Sellwood 2014; Grand et al. 2016). Finally, if the disc itself is a major cause for the depletion of substructures in the inner halo (D'Onghia et al. 2010) the substructures that interact with the disc are likely to be a biased subset of the entire substructure population. On the one hand, they are likely to be the most strongly stripped after they have interacted with the disc. On the other hand, if we measure the depletion of substructures after one or more passages, we may overestimate the depletion factor of the substructures at the time they interact with the disc.

7 SUMMARY

We have studied how baryonic effects can change the abundance of substructures in the mass range $M = 10^{6.5}$–$10^{8.5}\,M_{\odot}$ inside the Milky Way mass haloes of $M_{200} \sim 10^{12}\,M_{\odot}$ over a lookback time of up to 5 Gyr. We find that the abundance of subhaloes, independent of subhalo mass, is reduced in hydrodynamic simulations of the same host halo compared to their DMO counterpart. The depletion increases towards the halo centre: at $r > 50$ kpc, the number of subhaloes in the hydrodynamic simulations is above $3/4$ of that in the DMO counterparts, dropping to $\sim 1/2$ at $r < 10$ kpc. While baryonic effects of this magnitude clearly need to be taken into account for accurate predictions, they do not impede the detection of dark substructures through stream gaps, disc heating or lensing.

Purely in terms of substructure abundance, D'Onghia et al. (2010) found a stronger reduction, with the subhalo number reduced to $1/3$ relative to the original DMO simulation at $10^7\,M_{\odot}$ by the effects of the stellar disc alone. This is due in part to the much higher disc mass (10 per cent of M_{96}, or ~ 14 per cent of M_{200}) that they assumed. They also reported a significant subhalo mass dependence, with $1/2$ of subhaloes remaining at $10^9\,M_{\odot}$, while we find a nearly constant factor. One possible explanation for this may be numerical resolution: while we limit our study to subhaloes with more than 50 particles, the lower resolution in D'Onghia et al. (2010) means that $10^7\,M_{\odot}$ subhaloes only contain ~ 20 particles.

The central galaxies in our four simulations have stellar masses in the range $(1.2$–$2.8) \times 10^{10}\,M_{\odot}$, somewhat below the range of $\sim 5 \pm 1 \times 10^{10}\,M_{\odot}$ commonly assumed for the Milky Way (e.g. Flynn et al. 2006; Bovy & Rix 2013). For a greater stellar mass, we would expect some of the baryonic effects to increase, although we note that the decline in subhalo abundance relative to DMO simulations is due not only to the presence of the stellar component, but also to the contraction of the halo itself, as well as to the almost complete loss of baryons from low-mass haloes by reionization and ram-pressure stripping.

Although our results appear to be numerically converged, it is important to note that, independent of resolution, the identity and the properties of subhaloes are a matter of definition, and this work is no exception. The reduced substructure fraction in the halo centre is attributable in parts to the increasing background density. However, our principal results, the subhalo velocity distribution and the relative differences between the DMO and hydrodynamic simulations, should not be affected.

The processes that lead to a relative underdensity of subhaloes near the centre also give rise to a positive velocity bias and rising anisotropy of subhalo orbits, two effects we find enhanced in the hydrodynamic simulation. Furthermore, we find that the velocity distribution of substructures near the halo centre cannot be assumed to be Maxwellian. The preferential disruption of strongly bound subhaloes leads to velocity distributions with far fewer low-velocity subhaloes than commonly assumed, and while the few surviving low-velocity subhaloes near the halo centre have more circular orbits, the overall subhalo population near the centre is dominated by high-velocity subhaloes on highly radial orbits. This impacts both total number and strength of detectable substructure interactions.

REFERENCES

Amorisco N. C., Gòmez F. A., Vegetti S., White S. D. M., 2016, MNRAS, 463, L17
Arraki K. S., Klypin A., More S., Trujillo-Gomez S., 2014, MNRAS, 438, 1466
Avila-Reese V., Colín P., Valenzuela O., D'Onghia E., Firmani C., 2001, ApJ, 559, 516
Baumgardt H., Hut P., Heggie D. C., 2002, MNRAS, 336, 1069
Benson A. J., Lacey C. G., Baugh C. M., Cole S., Frenk C. S., 2002, MNRAS, 333, 156
Benson A. J., Lacey C. G., Frenk C. S., Baugh C. M., Cole S., 2004, MNRAS, 351, 1215
Binney J., Tremaine S., 2008, Galactic Dynamics, 2nd edn. Princeton Univ. Press, Princeton, NJ
Booth C. M., Schaye J., 2009, MNRAS, 398, 53
Bose S., Hellwing W. A., Frenk C. S., Jenkins A., Lovell M. R., Helly J. C., Li B., 2016, MNRAS, 455, 318
Bournaud F., Elmegreen B. G., Martig M., 2009, ApJ, 707, L1
Bovy J., Rix H.-W., 2013, ApJ, 779, 115
Bovy J., Erkal D., Sanders J. L., 2017, MNRAS, 466, 628
Boylan-Kolchin M., Bullock J. S., Kaplinghat M., 2011, MNRAS, 415, L40
Brooks A. M., Kuhlen M., Zolotov A., Hooper D., 2013, ApJ, 765, 22
Bullock J. S., Kravtsov A. V., Weinberg D. H., 2000, ApJ, 539, 517
Carlberg R. G., Grillmair C. J., 2013, ApJ, 768, 171
Chan T. K., Kereš D., Oñorbe J., Hopkins P. F., Muratov A. L., Faucher-Giguère C.-A., Quataert E., 2015, MNRAS, 454, 2981
Crain R. A. et al., 2015, MNRAS, 450, 1937
Croft R. A. C., Weinberg D. H., Bolte M., Burles S., Hernquist L., Katz N., Kirkman D., Tytler D., 2002, ApJ, 581, 20
Dalal N., Kochanek C. S., 2002, ApJ, 572, 25
Dalla Vecchia C., Schaye J., 2012, MNRAS, 426, 140
Davis M., Efstathiou G., Frenk C. S., White S. D. M., 1985, ApJ, 292, 371
Diemand J., Moore B., Stadel J., 2004, MNRAS, 352, 535
Diemand J., Kuhlen M., Madau P., 2007, ApJ, 667, 859
Dolag K., Borgani S., Murante G., Springel V., 2009, MNRAS, 399, 497
D'Onghia E., Springel V., Hernquist L., Keres D., 2010, ApJ, 709, 1138
Dutton A. A., Treu T., 2014, MNRAS, 438, 3594
Dutton A. A., Macciò A. V., Frings J., Wang L., Stinson G. S., Penzo C., Kang X., 2016, MNRAS, 457, L74
Erkal D., Belokurov V., 2015a, MNRAS, 450, 1136
Erkal D., Belokurov V., 2015b, MNRAS, 454, 3542
Fairbairn M., Schwetz T., 2009, J. Cosmol. Astropart. Phys., 1, 037

Fattahi A. et al., 2016, MNRAS, 457, 844
Feldmann R., Spolyar D., 2015, MNRAS, 446, 1000
Flynn C., Holmberg J., Portinari L., Fuchs B., Jahreiß H., 2006, MNRAS, 372, 1149
Geen S., Slyz A., Devriendt J., 2013, MNRAS, 429, 633
Ghigna S., Moore B., Governato F., Lake G., Quinn T., Stadel J., 2000, ApJ, 544, 616
Gilmore G. et al., 2012, The Messenger, 147, 25
Governato F. et al., 2010, Nature, 463, 203
Grand R. J. J., Springel V., Gómez F. A., Marinacci F., Pakmor R., Campbell D. J. R., Jenkins A., 2016, MNRAS, 459, 199
Grillmair C. J., Dionatos O., 2006, ApJ, 643, L17
Hänninen J., Flynn C., 2002, MNRAS, 337, 731
Hezaveh Y. D. et al., 2016, ApJ, 823, 37
Hopkins P. F., 2013, MNRAS, 428, 2840
Hopkins P. F., Cox T. J., Younger J. D., Hernquist L., 2009, ApJ, 691, 1168
Ibata R. A., Lewis G. F., Irwin M. J., Quinn T., 2002, MNRAS, 332, 915
Jenkins A., 2010, MNRAS, 403, 1859
Jenkins A., 2013, MNRAS, 434, 2094
Jiang L., Helly J. C., Cole S., Frenk C. S., 2014, MNRAS, 440, 2115
Johansson P. H., Naab T., Burkert A., 2009, ApJ, 690, 802
Jones E. et al., 2001, SciPy: Open source scientific tools for Python. Available at: http://www.scipy.org/
Kazantzidis S., Magorrian J., Moore B., 2004, ApJ, 601, 37
Kazantzidis S., Bullock J. S., Zentner A. R., Kravtsov A. V., Moustakas L. A., 2008, ApJ, 688, 254
Kennedy R., Frenk C., Cole S., Benson A., 2014, MNRAS, 442, 2487
Klypin A., Kravtsov A. V., Valenzuela O., Prada F., 1999, ApJ, 522, 82
Komatsu E. et al., 2011, ApJS, 192, 18
Kuhlen M., Weiner N., Diemand J., Madau P., Moore B., Potter D., Stadel J., Zemp M., 2010, J. Cosmol. Astropart. Phys., 2, 030
Küpper A. H. W., Balbinot E., Bonaca A., Johnston K. V., Hogg D. W., Kroupa P., Santiago B. X., 2015, ApJ, 803, 80
Lacey C. G., 1984, MNRAS, 208, 687
Libeskind N. I., Yepes G., Knebe A., Gottlöber S., Hoffman Y., Knollmann S. R., 2010, MNRAS, 401, 1889
Lovell M. R. et al., 2012, MNRAS, 420, 2318
LSST Science Collaboration et al., 2009, preprint (arXiv:0912.0201)
Macciò A. V., Moore B., Stadel J., Diemand J., 2006, MNRAS, 366, 1529
Mandelbaum R., Seljak U., Cool R. J., Blanton M., Hirata C. M., Brinkmann J., 2006, MNRAS, 372, 758
Mao S., Schneider P., 1998, MNRAS, 295, 587
Merritt D., 1985, AJ, 90, 1027
Metcalf R. B., Madau P., 2001, ApJ, 563, 9
Moster B. P., Macciò A. V., Somerville R. S., Johansson P. H., Naab T., 2010, MNRAS, 403, 1009
Navarro J. F., White S. D. M., 1994, MNRAS, 267, 401
Navarro J. F., Eke V. R., Frenk C. S., 1996, MNRAS, 283, L72
Nierenberg A. M., Treu T., Wright S. A., Fassnacht C. D., Auger M. W., 2014, MNRAS, 442, 2434
Ocvirk P. et al., 2016, MNRAS, 463, 1462
Odenkirchen M. et al., 2001, ApJ, 548, L165
Okamoto T., Gao L., Theuns T., 2008, MNRAS, 390, 920
Onions J. et al., 2012, MNRAS, 423, 1200
Osipkov L. P., 1979, Pisma v Astron. Z., 5, 77
Papastergis E., Martin A. M., Giovanelli R., Haynes M. P., 2011, ApJ, 739, 38
Perryman M. A. C. et al., 2001, A&A, 369, 339
Quinn P. J., Hernquist L., Fullagar D. P., 1993, ApJ, 403, 74
Rice S. O., 1945, Bell Syst. Tech. J., 24, 46
Romano-Díaz E., Shlosman I., Heller C., Hoffman Y., 2010, ApJ, 716, 1095
Rosas-Guevara Y. M. et al., 2015, MNRAS, 454, 1038
Sawala T., Frenk C. S., Crain R. A., Jenkins A., Schaye J., Theuns T., Zavala J., 2013, MNRAS, 431, 1366
Sawala T. et al., 2015, MNRAS, 448, 2941
Sawala T. et al., 2016a, MNRAS, 456, 85
Sawala T. et al., 2016b, MNRAS, 457, 1931
Schaller M. et al., 2015a, MNRAS, 451, 1247

Schaller M., Dalla Vecchia C., Schaye J., Bower R. G., Theuns T., Crain R. A., Furlong M., McCarthy I. G., 2015b, MNRAS, 454, 2277

Schaller M., Frenk C. S., Fattahi A., Navarro J. F., Oman K. A., Sawala T., 2016, MNRAS, 461, L56

Schaye J., Dalla Vecchia C., 2008, MNRAS, 383, 1210

Schaye J., Theuns T., Rauch M., Efstathiou G., Sargent W. L. W., 2000, MNRAS, 318, 817

Schaye J. et al., 2015, MNRAS, 446, 521

Schönrich R., Binney J., 2009, MNRAS, 399, 1145

Sellwood J. A., 2014, Rev. Mod. Phys., 86, 1

Sellwood J. A., Nelson R. W., Tremaine S., 1998, ApJ, 506, 590

Spergel D. N., Steinhardt P. J., 2000, Phys. Rev. Lett., 84, 3760

Springel V., 2005, MNRAS, 364, 1105

Springel V., White S. D. M., Tormen G., Kauffmann G., 2001, MNRAS, 328, 726

Springel V. et al., 2008, MNRAS, 391, 1685

Stewart K. R., Bullock J. S., Wechsler R. H., Maller A. H., 2009, ApJ, 702, 307

Strigari L. E., Frenk C. S., White S. D. M., 2014, AAS, preprint (arXiv:1406.6079)

The Dark Energy Survey Collaboration, 2005, preprint (astro-ph/0510346)

Tikhonov A. V., Klypin A., 2009, MNRAS, 395, 1915

Toth G., Ostriker J. P., 1992, ApJ, 389, 5

van der Walt S., Colbert S. C., Varoquaux G., 2011, Comput. Sci. Eng., 13, 22

Vande Putte D., Cropper M., Ferreras I., 2009, MNRAS, 397, 1587

Vegetti S., Lagattuta D. J., McKean J. P., Auger M. W., Fassnacht C. D., Koopmans L. V. E., 2012, Nature, 481, 341

Vegetti S., Koopmans L. V. E., Auger M. W., Treu T., Bolton A. S., 2014, MNRAS, 442, 2017

Vergados J. D., Hansen S. H., Host O., 2008, Phys. Rev. D, 77, 023509

Viel M., Becker G. D., Bolton J. S., Haehnelt M. G., 2013, Phys. Rev. D, 88, 043502

Vogelsberger M. et al., 2009, MNRAS, 395, 797

Walker M. G., Peñarrubia J., 2011, ApJ, 742, 20

Walker I. R., Mihos J. C., Hernquist L., 1996, ApJ, 460, 121

Wiersma R. P. C., Schaye J., Smith B. D., 2009a, MNRAS, 393, 99

Wiersma R. P. C., Schaye J., Theuns T., Dalla Vecchia C., Tornatore L., 2009b, MNRAS, 399, 574

Willett B. A., Newberg H. J., Zhang H., Yanny B., Beers T. C., 2009, ApJ, 697, 207

Wright E. L. et al., 1992, ApJ, 396, L13

Xu D. D. et al., 2009, MNRAS, 398, 1235

Xu D., Sluse D., Gao L., Wang J., Frenk C., Mao S., Schneider P., Springel V., 2015, MNRAS, 447, 3189

Yoon J. H., Johnston K. V., Hogg D. W., 2011, ApJ, 731, 58

Yurin D., Springel V., 2015, MNRAS, 452, 2367

Zhao H., 1996, MNRAS, 278, 488

Zhu Q., Marinacci F., Maji M., Li Y., Springel V., Hernquist L., 2016, MNRAS, 458, 1559

Zolotov A. et al., 2012, ApJ, 761, 71

APPENDIX A: HALO REFERENCE FRAME AND ORBITAL INTERPOLATION

A1 Host halo reference frame

Satellite subhaloes are typically tidally truncated at small radii, but the fact that their host haloes are extended structures complicates the choice of a reference frame. Because the centre of mass (CM) of a halo depends on material in the loosely bound outskirts, far away from the pericentres of satellites orbits, a more physical and more common definition of the host halo's position is the minimum of its gravitational potential, or more specifically, the position of the particle with the lowest potential energy, which we denote as CP.
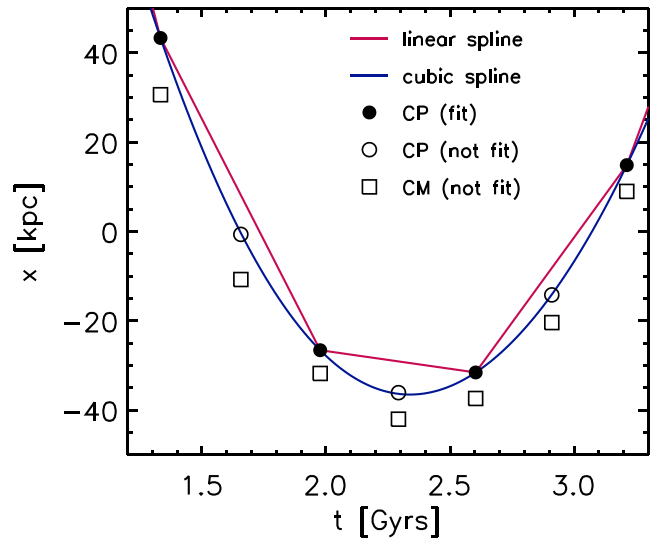

Figure A1. Evolution of the centre of potential (CP, circles) and centre of mass (CM, squares) of one of the host haloes, as a function of lookback time. For illustration, a linear least-squared fit to the centre of potential has been subtracted. The red and blue lines show a linear and a cubic fit to the CP at the times indicated by filled circles, the open symbols show intermediate times not used in the fit. The cubic spline accurately predicts the CP at the intermediate points to less than 1 kpc, while the distance between the CP and the CM can exceed 10 kpc.

Considering that the CM and centre of potential of a halo can differ by $\sim$10 kpc, for subhaloes that come much closer to the centre, the combination of CP positions and CM velocities is unsuitable, and can result in significant errors in the estimated orbital parameters. For this reason, in this work, we use the positions and velocities for both main halo and subhaloes relative to those of the CP $(\mathbf{x}_{CP}, \dot{\mathbf{x}}_{CP})$ where the time derivative $\dot{\mathbf{x}}_{CP}$ is obtained through higher order interpolation.

In Fig. A1, we show the evolution of the CP and CM of one of the host haloes during a time interval of $\sim$2 Gyr, with symbols indicating the values at individual snapshots, and lines showing the intermediate values obtained via interpolation. For illustration purposes, a linear least-squared fit to the CP has been subtracted from the reference frame. Red and blue lines show linear and cubic spline interpolations to those CP coordinates that are represented by filled circles. Open circles denote intermediate CP coordinates used only for validation of the interpolation. Using only half of the snapshots and cubic splines, the difference between the true and interpolated values of CP is under 1 kpc. As noted above, Fig. A1 also shows that the separation between the CM and CP can be $\sim$10 kpc, making the CM frame a poor choice for the motion of satellites in the inner tens of kpc of a halo.

A2 Orbit interpolations

In Fig. A2, we illustrate the importance of accurate orbital interpolation for measuring the orbital evolution, and hence the abundance and velocities of subhaloes near the halo centre. In the top panel, we show the positions of a subhalo near pericentre, relative to the host halo CP at five snapshots. Connecting lines show reconstructions of the orbit using linear (assuming constant velocity), and cubic (assuming acceleration that changes at most linearly) interpolations.

The bottom panel of Fig. A2 shows the distance of the satellite to centre as a function of time, resulting from the different
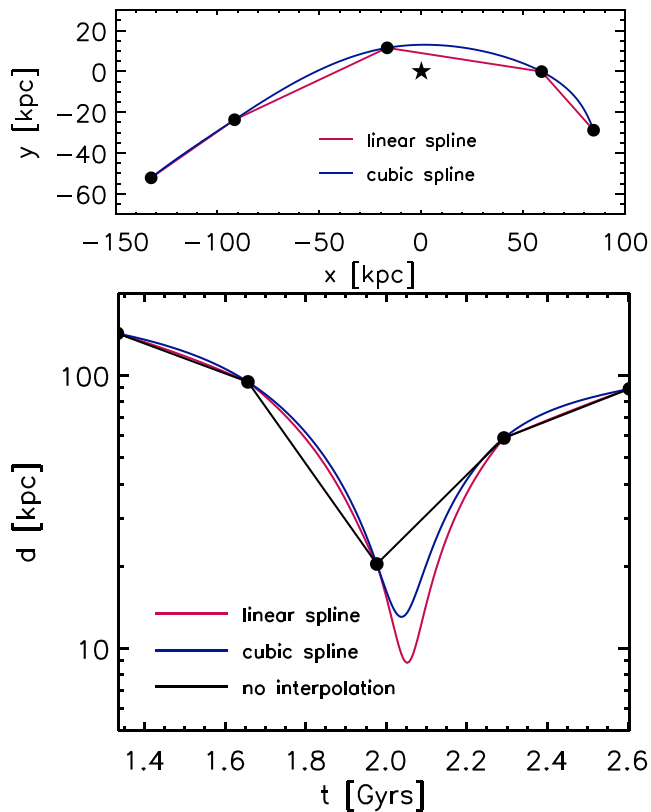
Figure A2. Top: circles denote positions at five snapshots of a subhalo near pericentre relative to the host halo CP marked by the star symbol. Positions in between snapshots are interpolated using linear (red) and third-order (blue) splines. Bottom: distance of the satellite to the host as a function of time, assuming no interpolation (black), or using the above interpolations with corresponding colours. Accurate estimates of the orbit near pericentre requires higher order interpolation; not interpolating overestimates the true pericentre distance, while linear interpolation underestimates it.

interpolation schemes, and also assuming no interpolation. Without interpolation, the measured pericentre distance is only an upper bound to the true value, so the abundance of subhaloes near the centre is almost always systematically underestimated. Using linear interpolation, the pericentre of a parabolic orbit is underestimated, unless the time intervals are so long that the entire pericentre passage is missed (consider, in the top panel of Fig. A2, a straight line between the first and final data points). As a result, with sufficiently small but finite timesteps, linear interpolation systematically underestimates the distance, and hence overestimates the abundance of substructures near the centre. Naturally, we have assumed that the reference frame, i.e. the host CP itself, is known accurately at all times; otherwise additional errors arise.

APPENDIX B: COMPARISON TO MAXWELLIAN AND GAUSSIAN VELOCITY DISTRIBUTIONS

In Fig. B1, we repeat the time-averaged probability density functions for the subhalo velocities, as shown in Fig. 8, and compare the fits used in this work to Gaussian and Maxwellian fits. It can be seen that, at large radii, the Rician and double-Gaussian distributions approach the Gaussian and Maxwellian approximations, but at small radii, the latter completely fail to reproduce the data.
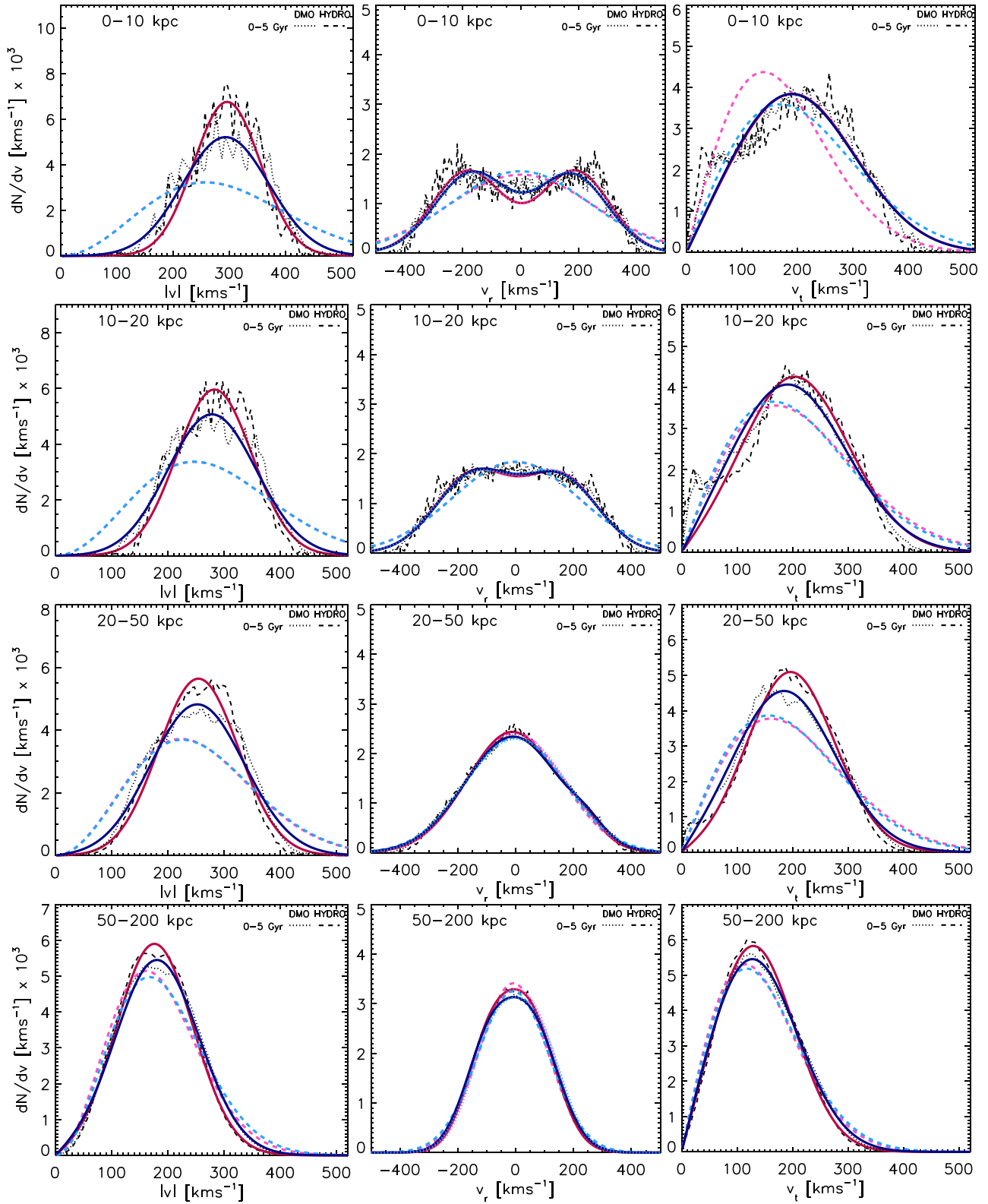
Figure B1. PDFs for $|v|$ (left column), v_r (middle column) and v_t (right column), as shown in Fig. 8, averaged over 5 Gyr in lookback time. Black dotted and dashed lines show our simulation results in the DMO and hydrodynamic simulations, respectively. Dark blue and dark red solid lines show the fits to double-Gaussian or Rician distribution functions to the DMO and hydrodynamic data, respectively, as described in Section 5. Lighter, dashed coloured lines show the corresponding fits to 3D-Maxwellians (for $|v|$, left column), a single Gaussian with free parameters μ and σ (for v_r, middle column) and to 2D-Maxwellians (for v_t, right column).

This paper has been typeset from a TEX/LATEX file prepared by the author.